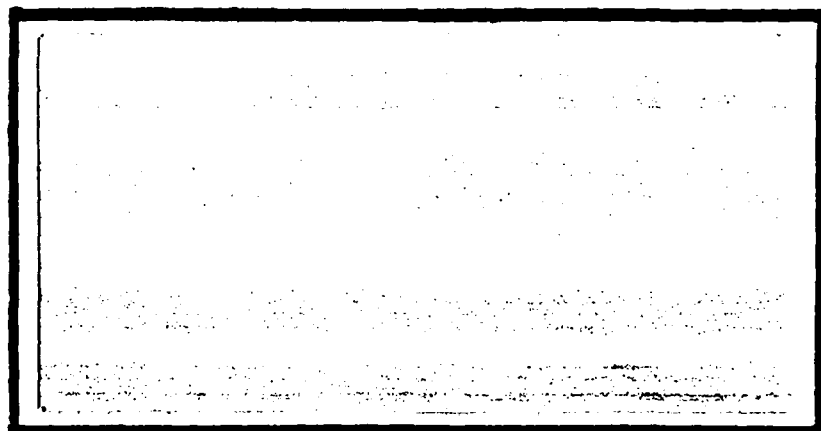


AD-A216 221

FILE COPY



DISTRIBUTION STATEMENT A

Approved for public release;
Distribution Unlimited

DTIC

ELECTE
JAN 02 1990

S

CD
E

D

DEPARTMENT OF THE AIR FORCE
AIR UNIVERSITY

AIR FORCE INSTITUTE OF TECHNOLOGY

Wright-Patterson Air Force Base, Ohio

90 01 02 109

AFIT/GAE/ENY/89D-24

NUMERICAL SIMULATION OF COMPRESSIBLE
VORTICES

THESIS

Scott Andrew Morton
First Lieutenant, USAF

AFIT/GAE/ENY/89D-24

Approved for public release; distribution unlimited

AFIT/GAE/ENY/89D-24

NUMERICAL SIMULATION OF COMPRESSIBLE VORTICES

THESIS

Presented to the Faculty of the School of Engineering
of the Air Force Institute of Technology
Air University
In Partial Fulfillment of the
Requirements for the Degree of
Master of Science in Aeronautical Engineering

Scott Andrew Morton, B.S.

First Lieutenant, USAF

December, 1989

Accession For	
NTIS	GRA&I
DTIC TAB	<input checked="" type="checkbox"/>
Unannounced	<input type="checkbox"/>
Justification	
By	
Distribution/	
Availability Codes	
Dist	Avail and/or
	Special
A-1	

Approved for public release; distribution unlimited

Acknowledgments

I would like to say thanks to my advisor, Capt Phil Beran for many insightful discussions concerning this work and fluids research in general. Thanks for the true friendship shown at times when my spirits were low and I was "looking at the tickets."

I would also like to say thanks to my sponsors Dr. Joseph Shang of the Air Force Flight Dynamics Lab and Dr. Robert Smith of the NASA Langley Research Center for supplying computer resources without which this work would not have been complete.

I am very grateful to my parents for all of their encouragement and prayers throughout this work, and most of all for teaching me that there are no bounds to what can be accomplished when one puts their faith and trust in the Lord Jesus Christ.

Finally, I would like to say thanks to my loving wife Carrie for putting up with many late nights and the shirking of husbandly duties so that I could complete this work. Many times she has taken care of endless details (that were most assuredly boring and extremely tiring) without a complaint.

Scott Andrew Morton

Table of Contents

	Page
Acknowledgments	ii
Table of Contents	iii
List of Figures	iv
Abstract	vi
I. Introduction	1-1
1.1 Historical Background	1-1
1.2 Problem Statement	1-3
1.3 Study Contributions	1-3
II. Mathematical Model	2-1
2.1 Model Assumptions	2-1
2.2 Governing Equations	2-4
2.3 Boundary Conditions	2-6
III. Solution Algorithm	3-1
3.1 Newton's Method	3-1
3.2 Pseudo-arc length Continuation	3-2
IV. Navier-Stokes Solutions	4-1
4.1 Grid Sensitivity Study	4-1
4.2 Comparison of Solutions for Low Mach Number	4-3
4.3 Flow Solutions at Various Mach Numbers	4-6
4.4 V Continuation at Various Mach Numbers	4-10

	Page
V. Conclusions and Recommendations	5-1
5.1 Solution Sensitivity to Boundary Conditions	5-1
5.2 Compressibility Trends	5-2
5.3 Recommendations for Follow-on Study	5-3
Appendix A. Derivation of the Governing Equations	A-1
Appendix B. Derivation of Representative Analytic Jacobian Elements . .	B-1
Bibliography	BIB-1
Vita	VITA-1

List of Figures

Figure	Page
2.1. Non-dimensional Sutherland's Formula, $T_0 = 298^\circ K$	2-3
2.2. Swirl velocity typical of trailing vortices, Beran (2)	2-6
2.3. Characterization of the flow, Beran (2)	2-7
2.4. Geometry of the computational domain, Beran (2)	2-8
3.1. Illustration of continuation procedure, Beran (2)	3-3
4.1. Effect of radial-node spacing on centerline axial velocity	4-2
4.2. Effect of axial-node spacing on centerline axial velocity	4-2
4.3. Effect of radial domain length on centerline axial velocity	4-3
4.4. Effect of axial domain length on centerline axial velocity	4-4
4.5. Comparison of centerline axial velocity profiles computed in four investigations for $Re = 200$ and $V = 1.0$	4-5
4.6. Continuation in Mach number, $Re = 200$ and $V = 1.0$	4-6
4.7. w profiles on the centerline for various Mach numbers, $Re = 200$ and $V = 1.0$	4-7
4.8. ρ profiles on the centerline for various Mach numbers, $Re = 200$ and $V = 1.0$	4-7
4.9. v profiles on the centerline for various Mach numbers, $Re = 200$ and $V = 1.0$	4-8
4.10. Continuation in V for $Re = 200$ and $M = 0.2$	4-10
4.11. Continuation in V for $Re = 200$ and $M = 0.4$	4-11
4.12. Continuation in V for $Re = 200$ and $M = 0.6$	4-11
4.13. Continuation in V for $Re = 200$ and $M = 0.2, 0.4$, and 0.6	4-12
4.14. w profiles on the centerline for various V 's at $Re = 200$ and $M = 0.8$. .	4-13
4.15. ρ profiles on the centerline for various V 's at $Re = 200$ and $M = 0.8$. .	4-14
B.1. Stencil used for discretization of the Continuity equation	B-2

List Of Symbols

Symbol	Definition
E_{Γ}	circulation perturbation norm
\underline{E}	system of nonlinear equations
\underline{F}_x	Jacobian matrix
I	number of nodes in the z direction
J	number of nodes in the r direction
K	coefficient of thermal conductivity
M	Mach number
P_r	Prandtl number
R	maximum distance in the r direction
Re	Reynolds number
T	temperature
T_0	freestream temperature
V	vortex strength
W	freestream velocity
Z	maximum distance in the z direction
c_p	specific heat
c_1, c_2	coefficients from linear μ - e relationship
d	arclength parameter
e	nondimensional internal energy
p	nondimensional pressure
r	radial coordinate
u	nondimensional radial velocity component
v	nondimensional swirl velocity component
w	nondimensional axial velocity component
\underline{x}	solution to the system of nonlinear equations
z	axial coordinate
Γ	circulation

γ	ratio of specific heats
δ_0	radius of the vortex core at the inflow
θ	swirl coordinate
λ	free parameter
μ	coefficient of viscosity
ρ	nondimensional density
τ	stress tensor

Abstract

A delta wing at a high angle of attack produces two vortices that generally undergo dramatic increases in core size, followed by the formation of regions of reversed flow. This phenomenon is called vortex breakdown and can have significant effects on the aircraft's lift, drag, and moment coefficients. The objective of this thesis is to provide a baseline model of the compressible vortex, independent of the complex body interaction with the delta wing. The model is then used to simulate vortex breakdown for various vortex strengths, Reynolds numbers, and Mach numbers with particular attention given to the effects of compressibility.

After running many simulations it was found that Mach number has a favorable effect by delaying vortex breakdown as defined above. Holding Reynolds number and vortex strength constant while increasing Mach number reduced the effective vortex strength while compressing the flow. Another important result of this compressible flow study was the disappearance of non-unique solutions at $Re = 200$ and $V = 1.0$ as Mach number was increased. No paths of non-unique solutions were found for $M > 0.2$.

NUMERICAL SIMULATION OF COMPRESSIBLE VORTICES

I. Introduction

Vortex breakdown is a phenomenon that occurs in rotational flows with a concentrated core of vorticity within a primarily irrotational flow. Swirling flows in pipes and leading-edge vortices over delta wings are examples of this flow. The term "vortex breakdown" is defined by Beran (2) as rotational flow with the development of a stagnation point on the core of a vortex, followed by a region of reversed flow and a dramatic increase in core size.

Vortex breakdown of the leading edge vortices over a delta wing can have significant effects on the aircraft's lift, drag, and moment coefficients. For this reason breakdown has been studied by many aerodynamicists since it was first discovered in 1957 by Peckham and Atkinson (33). A brief historical background and an outline of the study is contained in this chapter.

1.1 Historical Background

In the past thirty-two years since the discovery of vortex breakdown, there have been many experimental, analytical, and numerical investigations of the vortex breakdown problem. Several review papers have been written on the subject, most notably the reports by Hall (17), Leibovich (26), Leibovich (28), and Hall (14). After Peckham and Atkinson's discovery, Elle (5) and Lambourne and Bryer (25) conducted further experimental investigations of leading-edge vortices. Useful information was presented in these studies but quantitative results were difficult to obtain because of the sensitivity of the vortex core to probe disturbances.

Qualitative results were obtained by visualization, which led them to the discovery of two distinct types of vortex breakdown. In Hall's review (17), Figure 2 reproduces the picture taken by Lambourne and Bryer of vortex breakdown in the leading-edge vortices

over a delta wing. Flow visualization was made possible by injecting dye into the fluid at the wing apex. With this technique they discovered "bubble vortex breakdown" which is characterized by the near axisymmetric swelling of the core into the shape of a bubble, followed by turbulent disintegration of the vortex. The other type of breakdown found was "helical vortex breakdown" which can be described as an abrupt transformation of the linear core into a helical filament. Helical vortex breakdown occurs after several turns of the helical core.

The discovery of bubble vortex breakdown led several investigators to conduct swirling pipe flow experiments. The pipes were made of Plexiglass to permit flow visualization. The vortex strength and Reynolds number associated with the flow could be controlled in this apparatus by moving swirl vanes at the inflow and changing the mass flow rate respectively. This type of experiment was conducted by Harvey (18), Kirkpatrick (22), Sarpkaya (35), Sarpkaya (36), Sarpkaya (37), Faler and Leibovich (6), Garg (8), and Faler and Leibovich (7). Quantitative data was obtained by the last three through the use of laser doppler anemometry. By constraining the flow entering the test section to rotational symmetry, Faler and Leibovich (6) were able to classify seven distinct types of breakdown with five of them containing a stagnation point on the core, satisfying the earlier definition of vortex breakdown. The bubble type of breakdown was classified type 0, whereas the helical form was classified a type 2 breakdown.

The bubble form of breakdown was the most attractive type to simulate numerically due to its axisymmetric nature. It could be modeled in 2-D with a square computational grid, saving on computer resources. Kopecky and Torence (23) were the first to model vortex breakdown with the Navier-Stokes equations. Since 1973, results have been reported by Grabowski (11), Krause et al. (24), Nakamura et al. (31), Nakamura et al. (32), Hafez et al. (12), Beran (1), Hafez et al. (13), Brown and Lopez (3), Lopez (29), and Menne (30). Nakamura used the vortex filament method which allowed him to generalize the flow from rotational symmetry. The other papers assumed rotational symmetry in the model of the vortex breakdown. The papers by Brown and Lopez (3) and Lopez (29) compared computational results with experimental flow visualizations and found excellent agreement. All of these simulations have been accomplished using the assumption of incompressibility.

A compressible study of the vortex breakdown is a logical next step and is the subject of the present work.

1.2 Problem Statement

There are three main objectives of this study. The first is to extend the analysis of vortex breakdown into the regime of compressible flow, and to determine the trends of increasing Mach number. Since delta wing aircraft will certainly be operating in the compressible flow regime, a compressible study of the vortex breakdown, independent of the complex delta wing body interaction, is needed. This objective will be accomplished by obtaining a solution at a low freestream Mach number, M , with a particular set of Reynolds number, Re , and vortex strength, V , for which incompressible flow data is available and the vortex breakdown phenomenon occurs. A comparison is made with this data to validate the code, then calculations are made to obtain new solutions at increasing Mach number for the same values of Re and V .

The second objective is to investigate the effects of compressibility on the occurrence of non-unique solutions found by Beran (1). This objective will be accomplished by using Euler Newton pseudo-arc length continuation to map out the solution path as a function of vortex strength. This algorithm was developed by Keller (20) and is described in detail in Chapter III.

The third objective is to perform a grid sensitivity study. This objective is very important to investigators doing 3-D delta wing simulations. It will give these investigators information on the grid necessary to capture the vortex breakdown phenomenon accurately.

1.3 Study Contributions

This was a successful investigation because it outlined the effects of compressibility on axisymmetric vortex breakdown, not previously found in a body independent study. After running many simulations, it was found that Mach number has a favorable effect by destroying the vortex breakdown phenomenon. Holding Reynolds number and vortex strength constant, while increasing Mach number, eliminated vortex breakdown, while

compressing the fluid. Another important result of this compressible flow study was the disappearance of non-unique solutions as Mach number was increased. Non-unique solutions were reported in a previous incompressible flow study by Beran (1) at $Re = 200$ and $V = 1.0$. No paths of non-unique solutions were found in the compressible flow regime ($M > 0.3$).

II. Mathematical Model

In this study of the vortex breakdown, it was necessary to use the full Navier-Stokes (NS) model to capture the compressible, viscous nature of the trailing vortex. The model assumes subsonic, compressible flow, and thus it is not necessary to keep the convective terms in conservative form. The NS model consists of five equations and five unknowns: continuity, radial momentum, swirl momentum, axial momentum, and the energy equation. The equation of state was used to convert all other variables into the five unknowns: density, ρ , radial velocity, u , swirl velocity, v , axial velocity, w , and internal energy, e .

2.1 Model Assumptions

There were various assumptions used in the derivation of the NS model. Steady-state solutions were the object of this study and so $\frac{\partial(\cdot)}{\partial t}$ terms were set to zero. To simplify the equation of state, the perfect gas assumption was used with constant specific heat ratio $\gamma = 1.4$. This assumption is not a restrictive one because vortex breakdown has been observed experimentally at subsonic speeds. This argument also supports the assumption of Stoke's hypothesis, which is also good for subsonic speeds.

The temperature-viscosity relationship was derived by a linearization of Sutherland's formula:

$$\mu(T) = \frac{C_1 T^{3/2}}{C_2 + T}, \quad (2.1)$$

where for air at moderate temperatures $C_2 = 110.4^\circ K$ and C_1 need not be specified due to non-dimensionalization. First Sutherland's law was non-dimensionalized by $\mu(T_0)$, where T_0 is the temperature in the freestream:

$$\mu^* = \frac{\mu(T)}{\mu(T_0)} = \frac{C_1 T^{3/2}}{(C_2 + T)} \frac{(C_2 + T_0)}{C_1 T_0^{3/2}} = \left(\frac{T}{T_0}\right)^{3/2} \frac{(C_2/T_0 + 1)}{(C_2/T_0 + T/T_0)}. \quad (2.2)$$

Now, let $T^* = T/T_0$ and $C_2^* = C_2/T_0$, to obtain the non-dimensional Sutherland's formula:

$$\mu^*(T^*) = (T^*)^{3/2} \left(\frac{C_2^* + 1}{C_2^* + T^*} \right). \quad (2.3)$$

The solution algorithm requires that all variables appear in the numerator of the algebraic equations resulting from discretization of the NS model. For this reason, a linearization of equation 2.3 is obtained to ensure that T appears only in the numerator. A first order Taylor series expansion was used in the linearization process:

$$\mu^* = \mu^*(T_0^*) + \frac{d\mu^*}{dT^*} \bigg|_{T_0^*} \Delta T^* + O(\Delta T^*)^2, \quad (2.4)$$

where

$$\frac{d\mu^*}{dT^*} = \frac{(C_2^* + 1)}{(C_2^* + T^*)^2} \left[\frac{3}{2}(T^*)^{1/2}(C_2^* + T^*) - (T^*)^{3/2} \right], \quad (2.5)$$

but $T_0^* = \frac{T_0}{T_0} = 1$ and $\Delta T^* = T^* - T_0^* = T^* - 1$, so

$$\frac{d\mu^*}{dT^*} \bigg|_{T_0^*} = \left[\frac{3}{2} - \frac{1}{(C_2^* + 1)} \right] \quad (2.6)$$

which gives the non-dimensional linearized viscosity-temperature relationship:

$$\mu^*(T^*) = \left[\frac{3}{2} - \frac{1}{(C_2^* + 1)} \right] (T^* - 1) + 1. \quad (2.7)$$

A plot of equations 2.3 and 2.7 is given in Figure 2.1 to show the validity of this assumption. An analysis of the maximum difference in the linear μ^* relationship and Sutherland's μ^* relationship was accomplished. At $M = 0.4$ the maximum error was 0.33% and at $M = 0.8$ a maximum error of 2.0% was found.

The non-dimensional thermal conductivity-temperature relationship is derived from the Prandtl number relationship:

$$Pr = \frac{c_p \mu}{k} \quad (2.8)$$

where c_p and Pr are assumed constant for this study. Non-dimensionalization of μ and k by μ_0 and k_0 gives

$$Pr = \frac{c_p \mu^* \mu_0}{k^* k_0}, \quad (2.9)$$

but $\frac{c_p \mu_0}{k_0}$ also equals Pr so

$$Pr = \frac{\mu^*}{k^*} Pr, \quad (2.10)$$

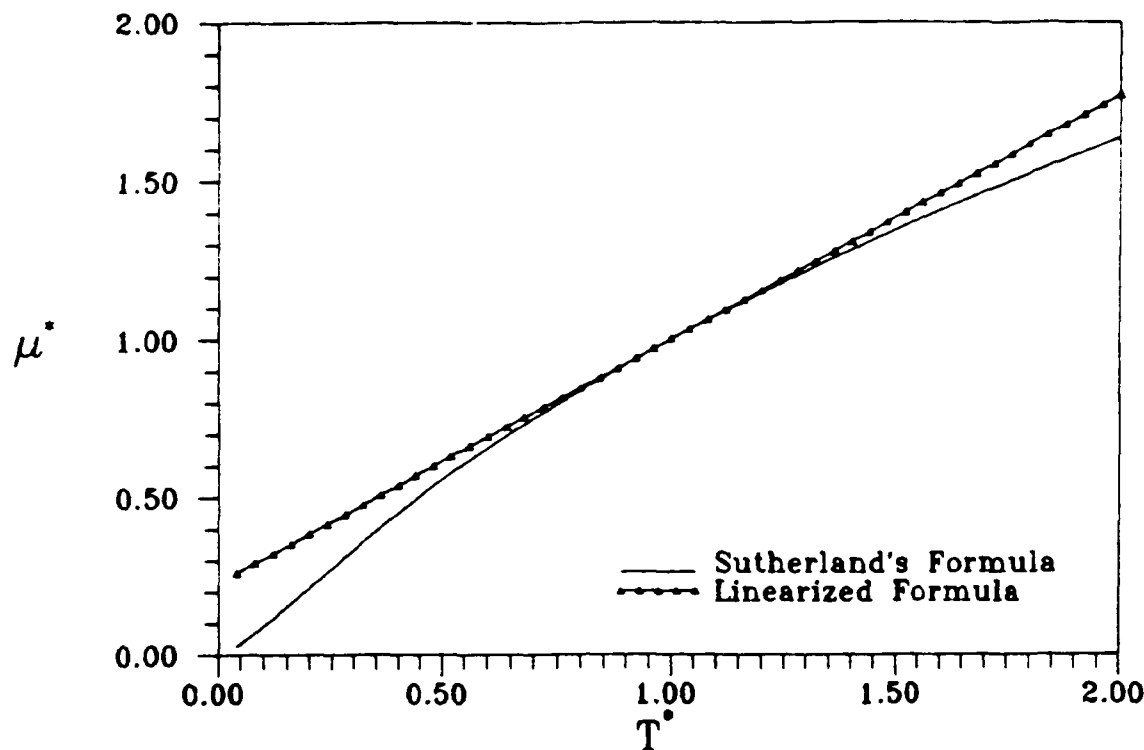


Figure 2.1. Non-dimensional Sutherland's Formula, $T_0 = 298^\circ K$

giving $k^* = \mu^*$.

Axisymmetry is also an assumption used in the governing equations. In experimental work two kinds of vortex breakdown have been observed: bubble vortex breakdown, and helical vortex breakdown. The bubble form is nearly axisymmetric, whereas the helical form is a fully 3-D phenomenon. In the interest of geometric simplicity, the bubble form is the subject of this thesis. The governing equations are cast in cylindrical form and then all partial derivatives with respect to θ are set to zero.

The last main assumption is laminar flow. No attempt was made at modeling turbulence, since this would add complications to an already complex flowfield. Vortex breakdown has been observed in laminar flow by previous investigators. In all numerical simulations Reynolds number was kept at 200, which is assumed to be in the laminar regime.

2.2 Governing Equations

In this section the non-dimensional, governing equations are presented. The derivation of these equations is accomplished using the assumptions from the previous section and can be found in Appendix A. The non-dimensionalized lengths were scaled by the radius of the vortex core at the inflow boundary, δ_0 , and velocities were scaled by the freestream velocity, W . Variables with subscripts r or z denote partial derivatives with respect to the independent variables. Following is a list of the five equations solved numerically.

Continuity:

$$(\rho u)_r + \frac{\rho u}{r} + (\rho w)_z = 0 \quad (2.11)$$

u Momentum:

$$\begin{aligned} \rho uu_r - \frac{\rho v^2}{r} + \rho w u_z + (\gamma - 1)(\rho e)_r = \\ \frac{1}{Re} [c_1 e_r (4/3 u_r - 2/3 \frac{u}{r} - 2/3 w_z) + c_1 e_z (u_z + w_r)] \\ + (c_1 e + c_2) (4/3 u_{rr} + 4/3 \frac{u_r}{r} - 4/3 \frac{u}{r^2} + u_{zz} + 1/3 w_{rz}) \end{aligned} \quad (2.12)$$

v Momentum:

$$\begin{aligned} \rho uv_r + \frac{\rho uv}{r} + \rho w v_z = \\ \frac{1}{Re} [c_1 e_r (v_r - \frac{v}{r}) + c_1 e_z (v_z)] \\ + (c_1 e + c_2) (v_{rr} + \frac{v_r}{r} - \frac{v}{r^2} + v_{zz}) \end{aligned} \quad (2.13)$$

w Momentum:

$$\begin{aligned} \rho uw_r + \rho uw_z + (\gamma - 1)(\rho e)_z = \\ \frac{1}{Re} [c_1 e_r (w_r + u_z) + c_1 e_z (-2/3 u_r - 2/3 \frac{u}{r} + 4/3 w_z)] \\ + (c_1 e + c_2) (1/3 u_{rz} + 1/3 \frac{u_z}{r} + w_{rr} + \frac{w_r}{r} + 4/3 w_{zz}) \end{aligned} \quad (2.14)$$

Energy:

$$\begin{aligned}
 & \gamma \left[\frac{\rho u \epsilon}{r} + (\rho u \epsilon)_r + (\rho u \epsilon)_z \right] + \frac{\rho_r}{2} [u^3 + u r^2 + u w^2] + \frac{\rho_z}{2} [u^2 w + r^2 w + w^3] \\
 & + \frac{\rho}{2} [(u^3)_r + (u r^2)_r + (u w^2)_r + (u^2 w)_z + (r^2 w)_z + (w^3)_z + \frac{u^3}{r} + \frac{u r^2}{r} + \frac{u w^2}{r}] = \\
 & \frac{1}{Re} [c_1 e_r (4/3 u u_r - 2/3 \frac{u^2}{r} - 2/3 u u_z + v v_r - \frac{v^2}{r} + u_z w + u w_r) \\
 & + c_1 e_z (u u_z + u w_r + v v_z - 2/3 u_r w - 2/3 \frac{u w}{r} + 4/3 w w_z) \\
 & + (c_1 \epsilon + c_2) (4/3 u_r^2 + 4/3 u u_{rr} - 4/3 u_r w_z + 1/3 u w_{rz} + 1/3 u_{rz} w + v_r^2 \\
 & + v v_{rr} - \frac{v v_r}{r} + 2 u_z w_r + w_r^2 + w w_{rr} + u_z^2 + u u_{zz} + v_z^2 + v v_{zz} \\
 & + 1/3 \frac{u_z w}{r} - 4/3 \frac{u w_z}{r} + 4/3 w_z^2 + 4/3 u w_{zz} - 2/3 \frac{u^2}{r} - \frac{v^2}{r} + \frac{w w_r}{r}) \\
 & + \frac{\gamma}{Pr} \left[(c_1 \epsilon + c_2) (\epsilon_{rr} + \epsilon_{zz} + \frac{e_r}{r}) + c_1 e_r^2 + c_1^2 \right] \quad (2.15)
 \end{aligned}$$

where $Re = \frac{W \delta a}{\nu}$, $M = \frac{W}{\sqrt{\gamma R T_0}}$, $Pr = c_p \frac{k_0}{k_0}$, and c_1 and c_2 are the constants obtained in linearization of Sutherland's formula and conversion of T^* to e :

$$c_1 = \left[3/2 - \frac{1}{c_2^2 + 1} \right] \gamma(\gamma - 1) M^2 \quad (2.16)$$

and

$$c_2 = 1 - \left[3/2 - \frac{1}{c_2^2 + 1} \right]. \quad (2.17)$$

Equations 2.11- 2.15 are then converted to a set of non-linear algebraic equations by means of second-order accurate central difference operators, and utilizing a constant grid spacing in both directions:

$$\delta_x u = \frac{u_{i+1} - u_{i-1}}{2 \Delta x} \quad (2.18)$$

$$\delta_x^2 u = \frac{u_{i+1} - 2u_i + u_{i-1}}{(\Delta x)^2}. \quad (2.19)$$

On the boundaries, second-order one-sided derivatives were used:

$$\delta_x u = \frac{3u_i - 4u_{i-1} + u_{i-2}}{2 \Delta x} \quad (2.20)$$

Since an approximation of the location of the outflow boundary is used, a second-order

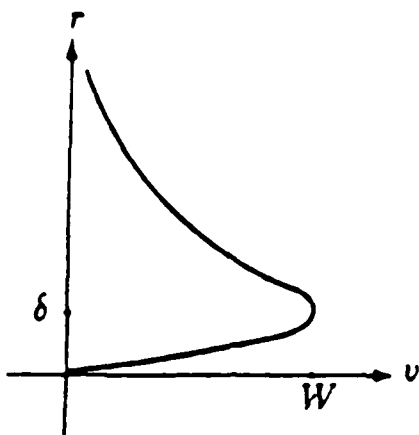


Figure 2.2. Swirl velocity typical of trailing vortices. Beran (2)

accurate difference at $I - \frac{1}{2}$ can be specified:

$$\delta_x u = \frac{u_i - u_{i-1}}{\Delta x}. \quad (2.21)$$

An example of the discretization process is given in Appendix B by applying these operators to the continuity equation. Once the governing equations are discretized the boundary conditions need to be specified to complete the set.

2.3 Boundary Conditions

The flow was assumed to be generated by a delta wing at a high angle of attack. The resulting trailing vortex is assumed to produce a swirl velocity profile downstream of the body approximated by Figure 2.2. This profile can be stated mathematically as

$$v = \begin{cases} Vr(2 - r^2) & r \leq 1 \\ V/r & r > 1 \end{cases}. \quad (2.22)$$

V becomes a free parameter of the model and is referred to as the vortex strength. When $V = 1$, the swirl velocity at the edge of the vortex core is equal to the freestream velocity W . The inflow boundary uses this swirl velocity profile, uniform axial velocity equal to

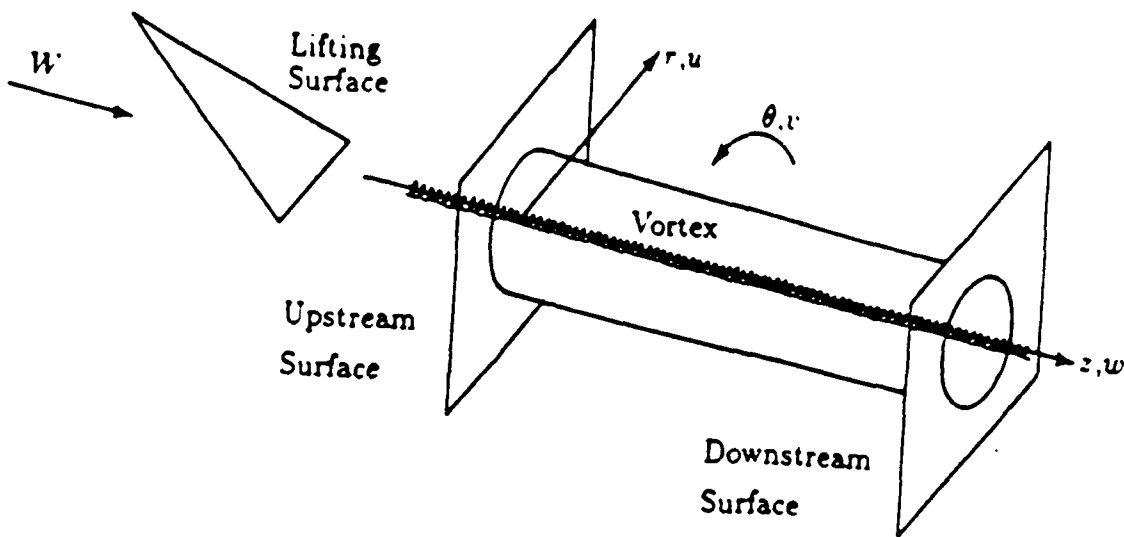


Figure 2.3. Characterization of the flow, Beran (2)

W , and radial velocity assumed to be zero. The physical domain is depicted in Figure 2.3 and the computational domain in Figure 2.4.

The radial boundary is assumed to be far enough away from the vortex axis for the axial velocity to return to freestream conditions. Also, swirl velocity is specified to be V/R and the radial velocity is specified in such a way as to satisfy continuity on the radial boundary. The outflow boundary is assumed to be far enough downstream for $\frac{\partial u}{\partial z} = 0$ for all of the dependent variables. The last boundary is the axis of symmetry and has velocity components u and v equal to zero, with a symmetry condition imposed on w , ($\frac{\partial w}{\partial r} = 0$).

The conditions on ρ and ϵ have not been described up to this point because different conditions were used in two phases of the investigation. In the first phase, the energy equation is replaced with $\rho = 1$ to simulate an incompressible flow. This causes ϵ to become a pressure term by the non-dimensional equation of state $p = (\gamma - 1)\rho\epsilon$. So the boundary conditions on ϵ become pressure boundary conditions. On the inflow boundary, $S1$, ϵ is determined by satisfying the u momentum equation on the boundary. On the radial

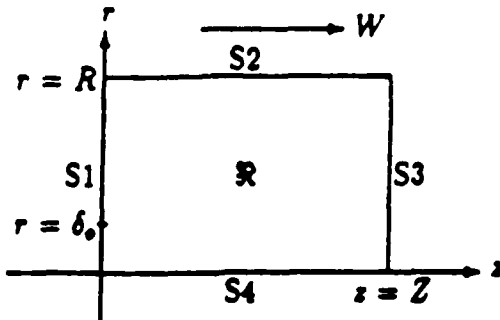


Figure 2.4. Geometry of the computational domain. Beran (2)

boundary S2, $\epsilon = 0$ which gives $p=0$ (freestream pressure). Outflow boundary S3 has the condition $\frac{\partial \epsilon}{\partial z} = 0$. The symmetry condition $\frac{\partial \epsilon}{\partial r} = 0$ is imposed on the axial boundary S4.

In the second phase, compressible flow, without the constant density assumption, was modeled. The compressible, columnar-flow equations were solved to determine an approximate density profile. Internal energy is not specified explicitly, instead the condition $\frac{\partial u}{\partial z} = 0$ is used to enforce a peak at the inflow. On the S2 boundary, $\rho = 1$ is again specified, and a Dirichlet condition on ϵ is derived from the equation of state with $T^* = 1$:

$$\epsilon = \frac{1}{\gamma(\gamma - 1)M^2}. \quad (2.23)$$

The S3 and S4 boundaries are treated in the same manner as in the first phase of the study.

Table 2.1. Phase 2 Boundary Conditions

Boundary S1	Boundary S2	Boundary S3	Boundary S4
$\rho = \rho_0$	$\rho = 1$	$\rho_z = 0$	$\rho_r = 0$
$u = 0$	$(\rho u)_r + \frac{\rho u}{r} = 0$	$u_z = 0$	$u = 0$
$v = Vr(2 - r^2) \quad r \leq 1$ $v = V/r \quad r > 1$	$v = V/R$	$v_z = 0$	$v = 0$
$w = 1$	$w = 1$	$w_z = 0$	$w_r = 0$
$w_z = 0$	$e = \frac{1}{\gamma(\gamma-1)M^2}$	$e_z = 0$	$e_r = 0$

These boundary conditions were developed through trial and error and a more informative discussion on boundary conditions can be found in Section 5.1. This section is intended only to present the boundary conditions used in the study. A summary of the boundary conditions used in phase 2 are in Table 2.1.

III. Solution Algorithm

One of the objectives of this study is to be able to determine if non-unique solutions of the flow equations exist. To compute non-unique solutions, a very robust algorithm is needed to obtain both stable and unstable, steady-state solutions. Newton's method is capable of computing non-unique solutions for the set of non-linear, algebraic equations resulting from a discretization of equations 2.11- 2.15.

Newton's method is guaranteed to converge if the initial guess is within its ball of convergence (19). The difficulty is finding an initial guess within the ball. At higher values of Reynolds number and vortex strength, the ball of convergence can contract making it more and more difficult to find a suitable initial guess. To overcome this problem pseudo-arclength continuation is used in combination with Newton's method. Pseudo-arclength continuation, like other continuation methods, uses information at the current solution to calculate a solution at a parameter value close by. This chapter is dedicated to describing these two methods.

3.1 Newton's Method

Newton's method is an iterative algorithm that solves the nonlinear system of equations

$$F(\underline{x}; \lambda) = 0. \quad (3.1)$$

Given \underline{x}^i , an initial approximation to the solution vector \underline{x} , and λ the free parameter, an improved approximation \underline{x}^{i+1} can be found by solving the system of equations:

$$E_{\underline{x}}(\underline{x}^i; \lambda) (\underline{x}^{i+1} - \underline{x}^i) = -F(\underline{x}^i; \lambda). \quad (3.2)$$

The solution to equation 3.2 is known as a Newton iterate. Successive Newton iterates are computed until the norm of E goes to zero, usually defined as machine precision or some other tolerably small value. The norm used is defined as:

$$\|E\| = \left(\sum_{k=1}^N \Delta r \Delta z F_k^2(\underline{x}^{i+1}; \lambda) \right)^{1/2}. \quad (3.3)$$

\underline{F}_x is the Jacobian matrix, which is defined as:

$$\underline{F}_x \equiv \left[\frac{\partial F_i}{\partial x_j} \right]. \quad (3.4)$$

An example calculation of some of the elements of equation 3.4 is shown in Appendix B. Newton's method is an attractive algorithm because of its ease of programming and its convergence rate. The method is guaranteed to converge quadratically if the Jacobian matrix is non-singular and the initial guess is within the ball of convergence (19). No singular matrices were encountered during any of the runs and pseudo-arc length continuation was used to find a suitable initial guess.

3.2 Pseudo-arc length Continuation

It has been proven that if a solution \underline{x}^* is known and \underline{F}_x^* is nonsingular, then for some range of λ about λ^* there exists a unique solution path through $(\underline{x}^*, \lambda^*)$. The proof is outlined in (21). Pseudo-arc length continuation (PAC) is Keller's method of computing solutions along the solution path by using information at $(\underline{x}^*, \lambda^*)$ to compute the next solution point.

Figure 3.1 is representative of a solution path found by plotting the norm of the solution vector versus the free parameter λ . The PAC process is to compute a tangent vector \underline{T} at the known solution \underline{x}^* , designated as P . Then, at a distance d away, search along a line perpendicular to \underline{T} for the next solution point. This is done by first using arclength to parameterize the solution path ($\underline{x} = \underline{x}(s)$, $\lambda = \lambda(s)$, and $\underline{F} = \underline{F}(s) = 0$). Then the tangent vector is computed by

$$\frac{d}{ds} \underline{F}(\underline{x}(s); \lambda(s)) = 0. \quad (3.5)$$

Using the chain rule equation 3.5 becomes

$$\underline{F}_x(s) \dot{\underline{x}}(s) + \underline{F}_\lambda(s) \dot{\lambda}(s) = 0. \quad (3.6)$$

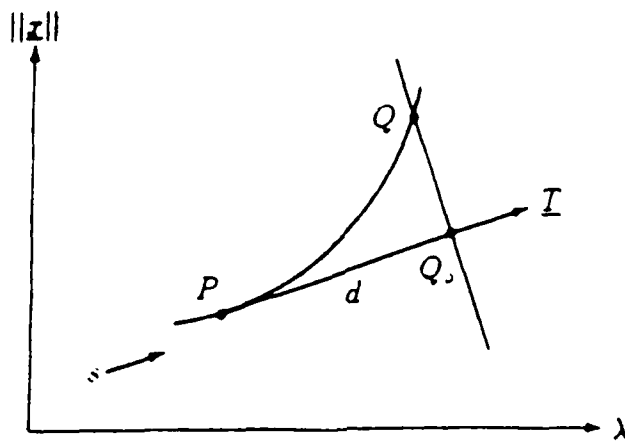


Figure 3.1. Illustration of continuation procedure, Beran (2)

where

$$\dot{\underline{x}}(s) \equiv \frac{d\underline{x}}{ds}(s) \quad (3.7)$$

and

$$\dot{\lambda}(s) \equiv \frac{d\lambda}{ds}(s). \quad (3.8)$$

The definition of arclength is

$$\| \dot{\underline{x}}(s) \|^2 + \dot{\lambda}^2(s) = 1. \quad (3.9)$$

Equations 3.6 and 3.9 can then be solved as a system for the tangent vector:

$$\underline{T}(s) = \begin{pmatrix} \dot{\underline{x}}(s) \\ \dot{\lambda}(s) \end{pmatrix}, \quad (3.10)$$

providing the Jacobian matrix is not singular. Now define $\underline{\phi}$ such that

$$\underline{\phi} = \underline{F}_{\underline{x}}^{-1}(s) \underline{F}_{\lambda}(s). \quad (3.11)$$

Then equations 3.6 and 3.9 give the following relationships

$$\dot{\lambda}(s) = \frac{\pm 1}{\sqrt{1 + \|\phi\|^2}} \quad (3.12)$$

and

$$\dot{\underline{z}}(s) = -\dot{\lambda}(s)\underline{\phi}. \quad (3.13)$$

The sign of equation 3.12 represents the direction of the tangent vector and is therefore indeterminate. At the startup of the continuation process this sign is set depending on which part of the solution path is to be computed.

From the solution P , the tangent vector T , and the distance d , the initial solution vector Q_0 can be computed:

$$\begin{pmatrix} \underline{z} \\ \lambda \end{pmatrix}_{Q_0} = \begin{pmatrix} \underline{z} \\ \lambda \end{pmatrix}_P + d \begin{pmatrix} \dot{\underline{z}} \\ \dot{\lambda} \end{pmatrix}_P. \quad (3.14)$$

The solution Q lies on a line perpendicular to T passing through Q_0 . This condition can be stated mathematically as

$$D \equiv \dot{\underline{z}}_P^T(\underline{z}_Q - \underline{z}_P) + (\lambda_Q - \lambda_P)\dot{\lambda}_P = d \quad (3.15)$$

and can be added to the system of nonlinear equations 3.1. This new system is then solved by Newton's method with Q_0 as the initial guess. Q_0 becomes a better and better first approximation as d gets smaller. The solution \underline{z}_Q is obtained when $F = 0$ and $D = d$. Another solution can be computed by repeating the process.

For the vortex breakdown problem, the most informative graphical representation of the solution path is found by plotting the free parameter Re , V , or M against the weighted L2 norm of the change in $\Gamma_{(i,j)}$ from the inflow $\Gamma_{0(j)}$:

$$E_\Gamma \equiv \left(\Delta r \Delta z \sum_{i=1}^I \sum_{j=1}^J (\Gamma_{(i,j)} - \Gamma_{0(j)})^2 \right)^{\frac{1}{2}}. \quad (3.16)$$

where $\Gamma_{(i,j)} = r_j v_{i,j}$. E_Γ is referred to as the "circulation perturbation" norm.

IV. Navier-Stokes Solutions

In Chapter *II*, a model for compressible trailing vortices was developed utilizing the Navier Stokes equations. After discretization, the equations became a set of non-linear algebraic equations. Using the method of solution described in Chapter *III*, solutions to the system of equations at $Re = 200$ for various vortex strengths and Mach numbers were computed and are presented in this chapter, as well as the solution paths computed by continuation in V and M . A grid sensitivity study and validation of the code with previous work are also presented.

4.1 Grid Sensitivity Study

In numerical studies, it becomes very important to show the degree to which the finite difference solution is independent of the grid used. Also, when using the far field as a boundary, the effect of computational domain size on the solution should also be analyzed. This section consists of a grid refinement and domain size study.

Both the studies were completed by computing solutions at $Re = 200$, $V = 1.0$, and $M = 0.15$, since reversed flow occurs at this set of parameters. In the grid refinement study the maximum radial and axial distances were held constant at $R = 2$ and $Z = 20$ while the number of nodes was varied. Radial grid refinement was analyzed by holding the nodes in the z direction constant at $I = 105$ and varying the number of nodes in the r direction J , depicted in Figure 4.1. At approximately $J = 27$, the solution becomes practically independent of increasing J . Next, z grid refinement was studied by varying I while holding $J = 27$, depicted in Figure 4.2. The solution points are coincidental for $I = 157$ and $I = 209$. The $I = 105$ solution produces very slight differences from the other two solutions.

In the domain size study the node spacing $\Delta r = \frac{R}{(J-1)}$ and $\Delta z = \frac{Z}{(I-1)}$ were kept approximately constant with R and Z varied. The study of radial domain size was difficult to obtain, because as J is increased by one the bandwidth of the system increases by 10 making the $J = 40$ case a computational limit for the available resources. Figure 4.3 shows the comparison and although only two solutions are shown ($R = 2$ and $R = 3$), there is

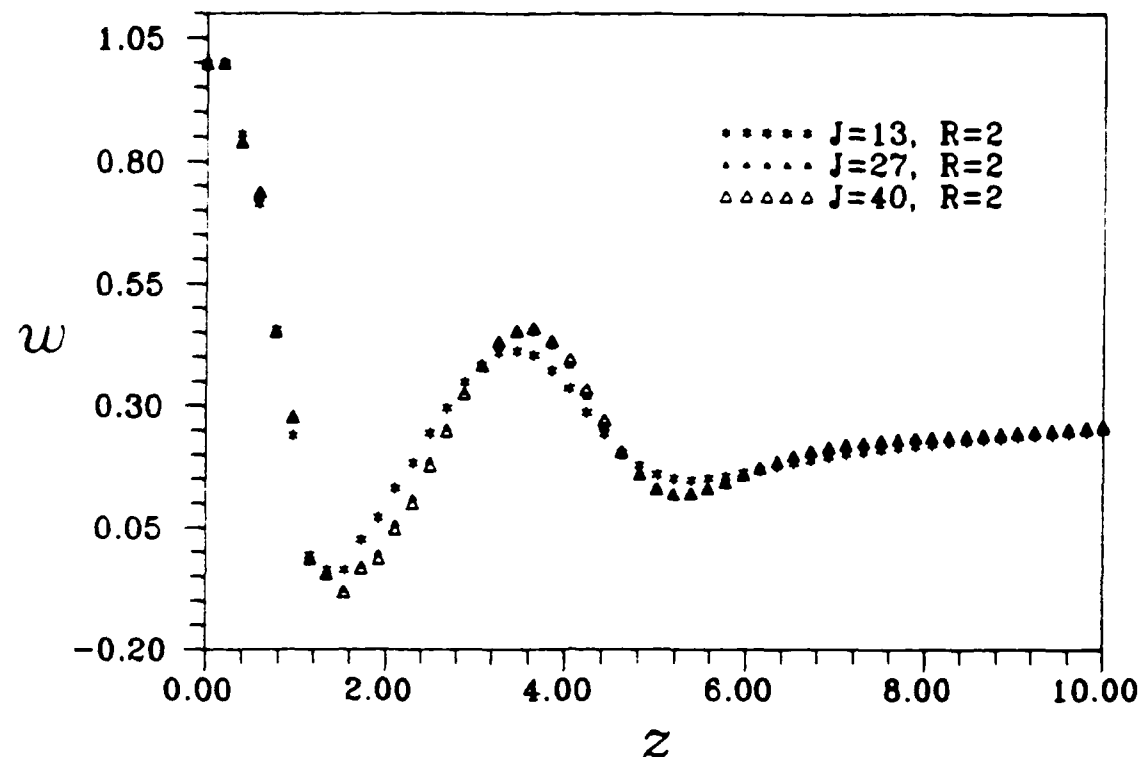


Figure 4.1. Effect of radial-node spacing on centerline axial velocity

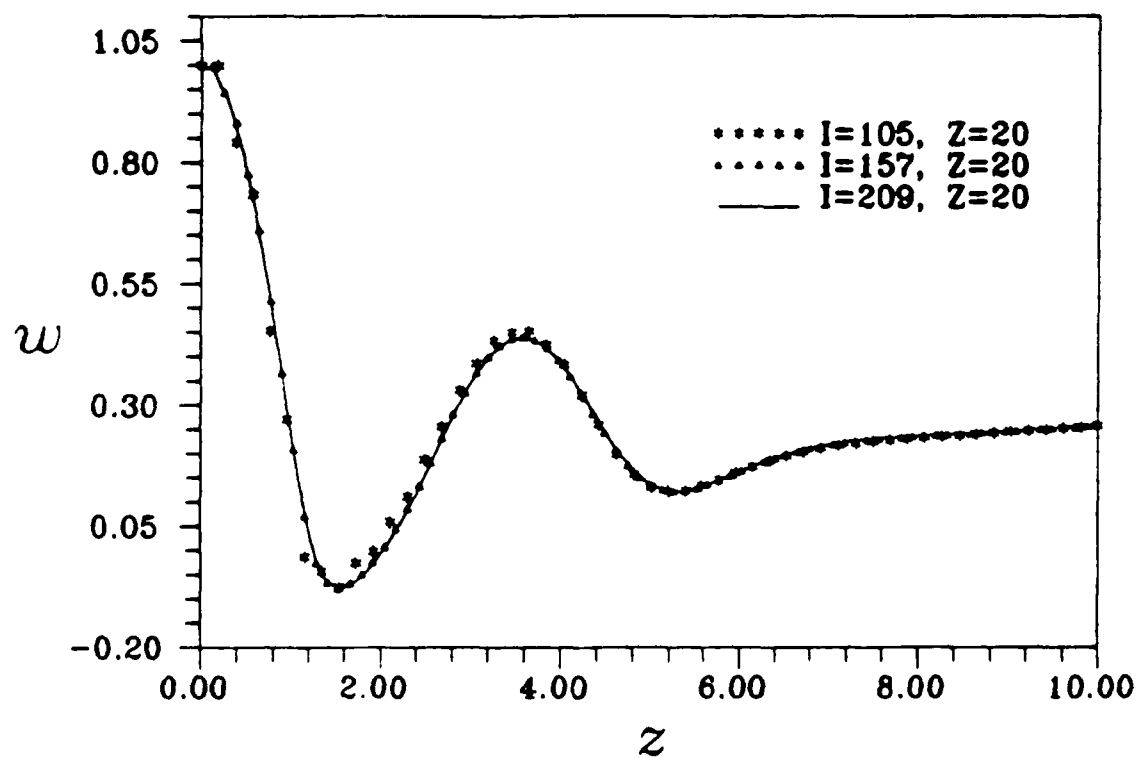


Figure 4.2. Effect of axial-node spacing on centerline axial velocity

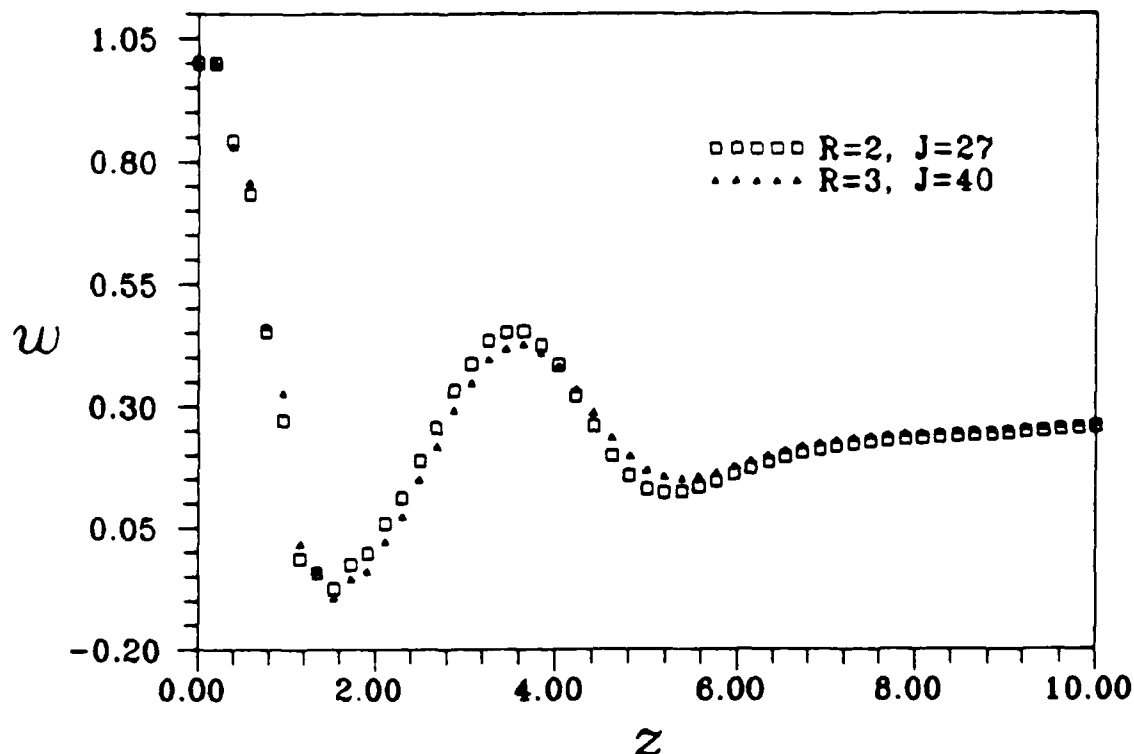


Figure 4.3. Effect of radial domain length on centerline axial velocity

only a slight difference between them. The $R = 2$ solution has a slightly higher peak value followed by a slightly lower minimum. The axial length study was more definitive and is shown in Figure 4.4. At $Z = 20$ and $I = 105$, the solution becomes independent of axial domain length. In summary, the solution becomes practically independent of domain size and node spacing at $R = 3$, $J = 40$, $Z = 20$, and $I = 157$. This would be the grid to choose if unlimited computer resources were available, but this was not the case for this study. Instead, the standard grid used throughout the study is $R = 2$, $J = 27$, $Z = 20$, and $I = 105$. This grid is a very good compromise and has only slight quantitative differences.

4.2 Comparison of Solutions for Low Mach Number

Steady-state axisymmetric, trailing vortices modeled with the Navier Stokes equations were studied previously by Grabowski (11), Hafez et al. (12), Beran (1), Hafez et al. (13), and Beran (2). Although each study modeled trailing vortices in essentially the

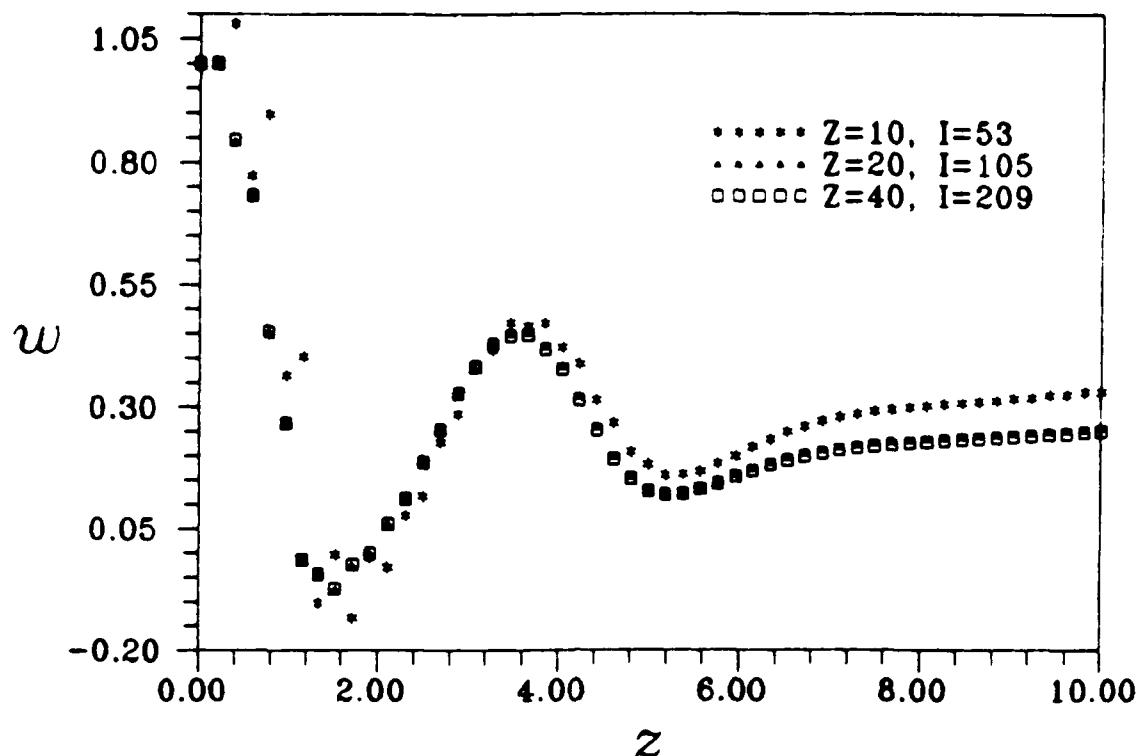


Figure 4.4. Effect of axial domain length on centerline axial velocity

same way, there were significant differences in the form of the governing equations, the finite difference expressions used, and the method of solution.

Grabowski cast the governing equations in primitive variable form, similar to this work, but he used a non-uniform grid with refinement near the axis of symmetry. The equations were integrated in time until convergence, utilizing the artificial compressibility method of Chorin (4). Hafez et al. (12) took a different approach. He used the stream function, vorticity, and circulation form, approximating derivatives with upwind differences at constant node spacing. An iterative relaxation technique was used to solve the set of equations. Beran (1), Hafez et al. (13), and Beran (2) also used the stream function, vorticity, and circulation form with constant node spacing, but the method of solving the equations essentially follows Chapter III of this work.

All of these studies were performed with the assumption of $M = 0$, whereas $M = 0.15$ in the current study. This Mach number was the lowest attainable due to numerical difficulties. This proved to be a very small portion of the difference as seen through

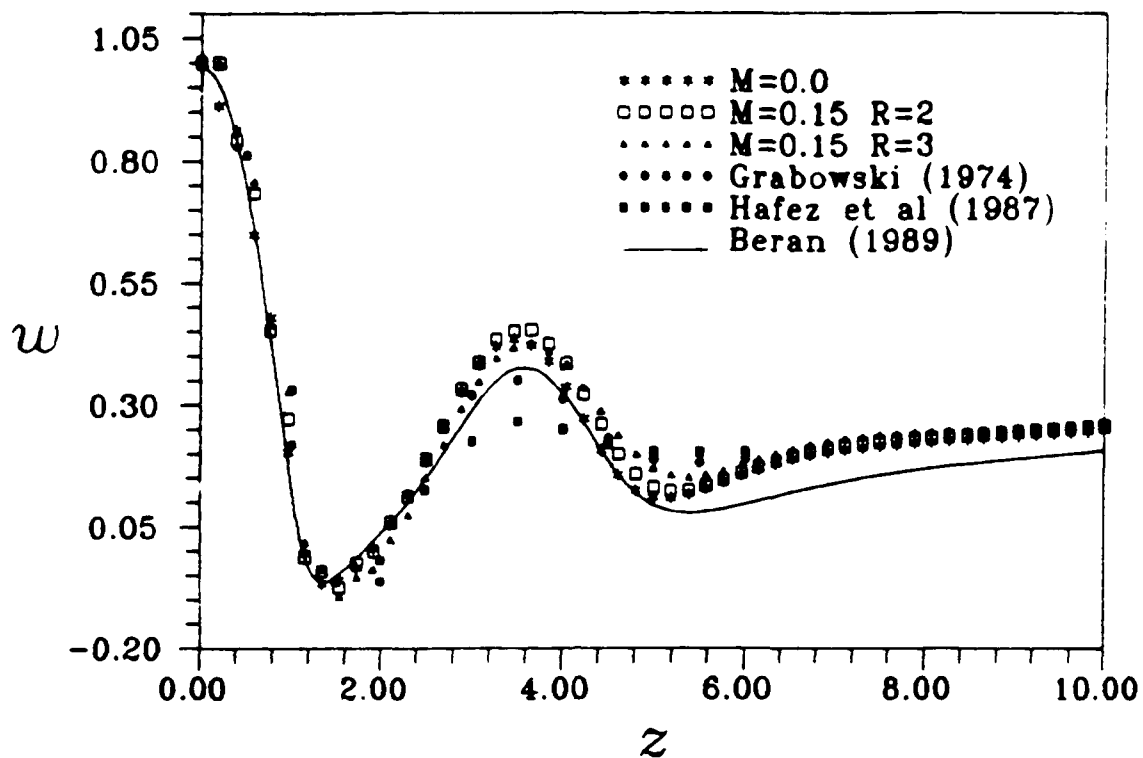


Figure 4.5. Comparison of centerline axial velocity profiles computed in four investigations for $Re = 200$ and $V = 1.0$

comparison with the phase 1, $M = 0$ code. The qualitative and quantitative behavior will now be compared for $Re = 200$ and $V = 1$. These conditions were chosen because vortex breakdown does occur and data is available from other studies for these conditions.

Figure 4.5 shows the comparison of these data sets. Solutions are in good agreement until $z = 2.5$. For $2.5 \leq z \leq 6$ all five curves are in what is termed as phase, with variations in peak value. Most notably Hafez et al. (13) has a much lower minimum value than the others. Beran (2) and Grabowski (11) are slightly lower in peak value. For $z > 6$ the present work, Grabowski (11), and Hafez et al. (13) show excellent agreement. Beran (2) returns to a lower value of axial velocity. Quantitatively the $M = 0.15$ and $R = 3$ solution and Grabowski (11) are in very good agreement, this is not surprising since Grabowski also cast his equations in primitive variable form, whereas Beran and Hafez used the stream function, vorticity, and circulation formulation. Qualitatively the current study and the three previous studies all show the same damped oscillatory behavior with a match in

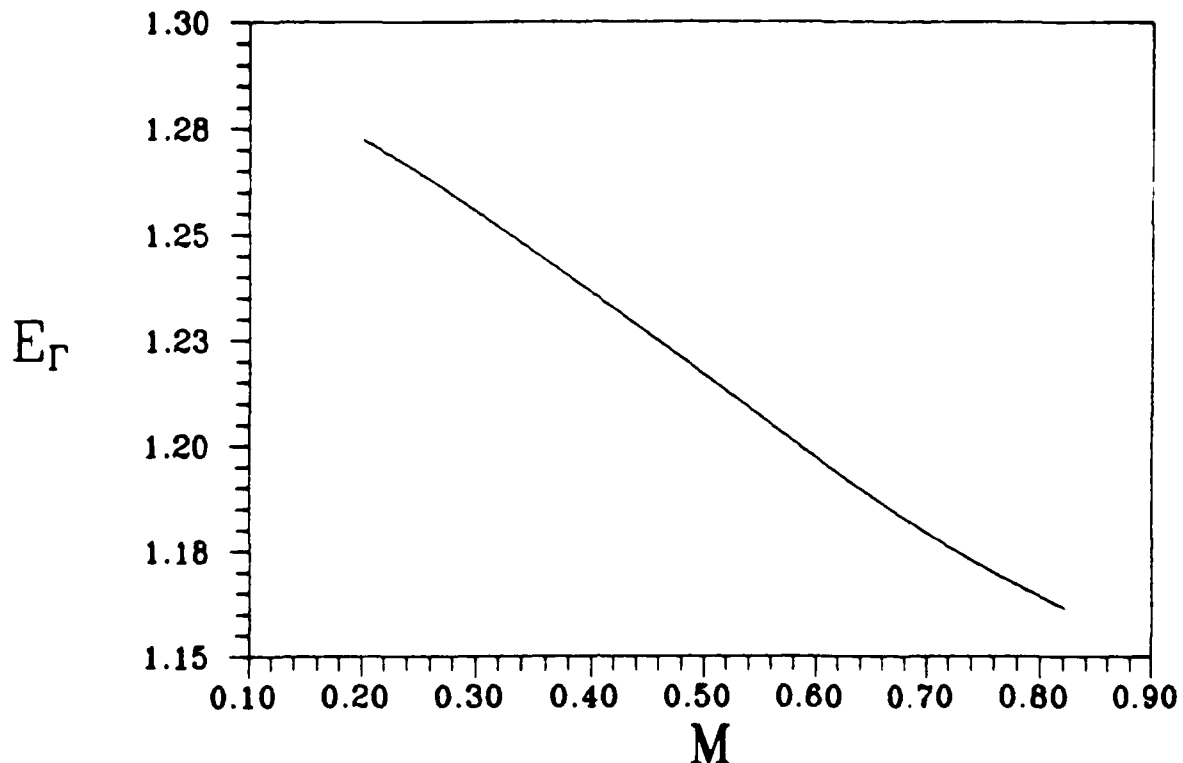


Figure 4.6. Continuation in Mach number, $Re = 200$ and $V = 1.0$

phase. With this kind of agreement, the code developed in this study may be accepted as a viable tool to study the effects of compressibility.

4.3 Flow Solutions at Various Mach Numbers

In this section solutions at varying Mach numbers are examined. A continuation in Mach number was performed over the range $0.2 \leq M \leq 1.0$ with $Re = 200$ and $V = 1.0$. In all of these runs the standard grid $I = 105$, $Z = 20$, $J = 27$, and $R = 2$ was used. Figure 4.6 presents E_Γ versus M for the continuation run. As one can see from this figure, the behavior is very regular as Mach number is varied. No limit points were encountered and the sign of the determinant of the Jacobian matrix was constant for the complete run suggesting no change in stability.

To analyze the effect of increasing Mach number, axial profiles of w and ρ on the centerline are presented in Figures 4.7 and 4.8. In the w profiles, one can see that as Mach number increases reversed flow is quickly lost and the breakdown is lost entirely at about

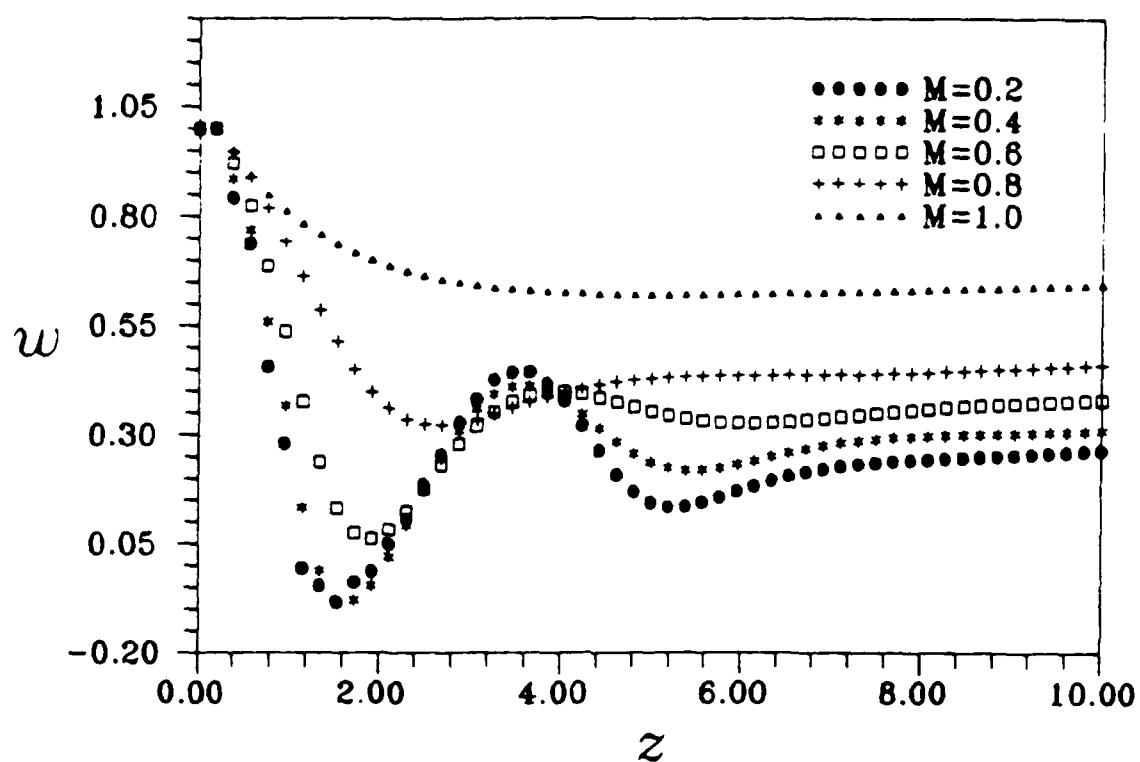


Figure 4.7. w profiles on the centerline for various Mach numbers, $Re = 200$ and $V = 1.0$

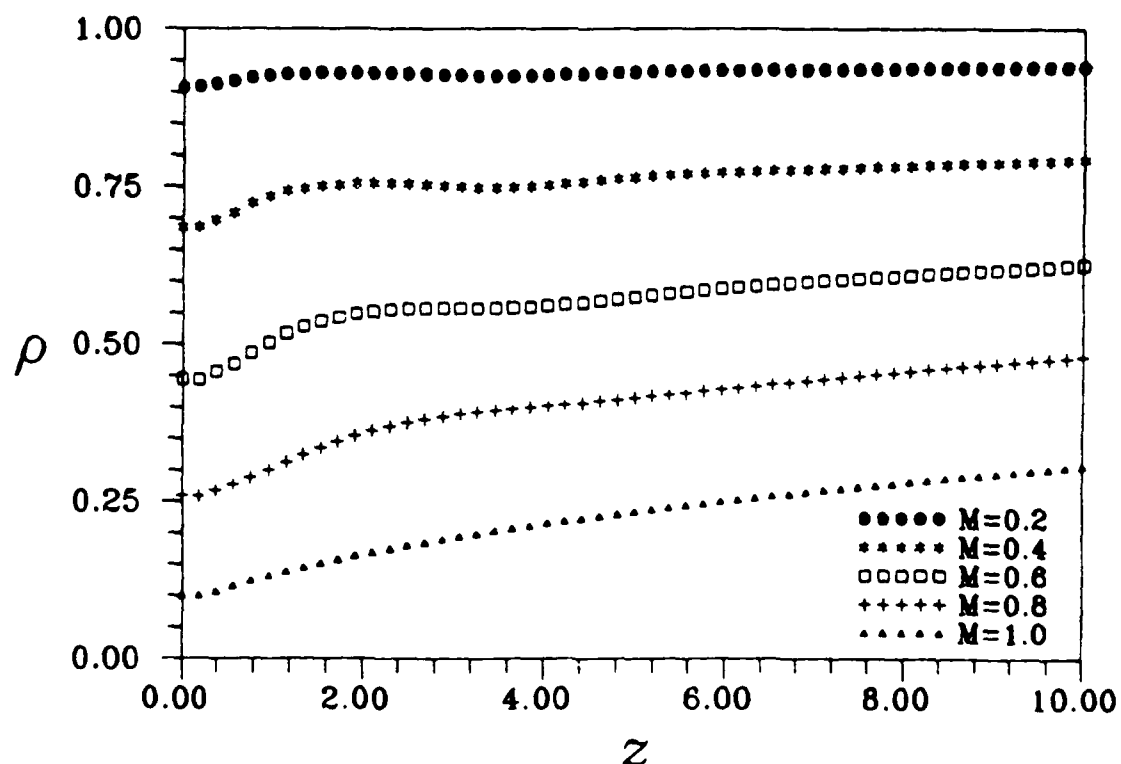


Figure 4.8. ρ profiles on the centerline for various Mach numbers, $Re = 200$ and $V = 1.0$

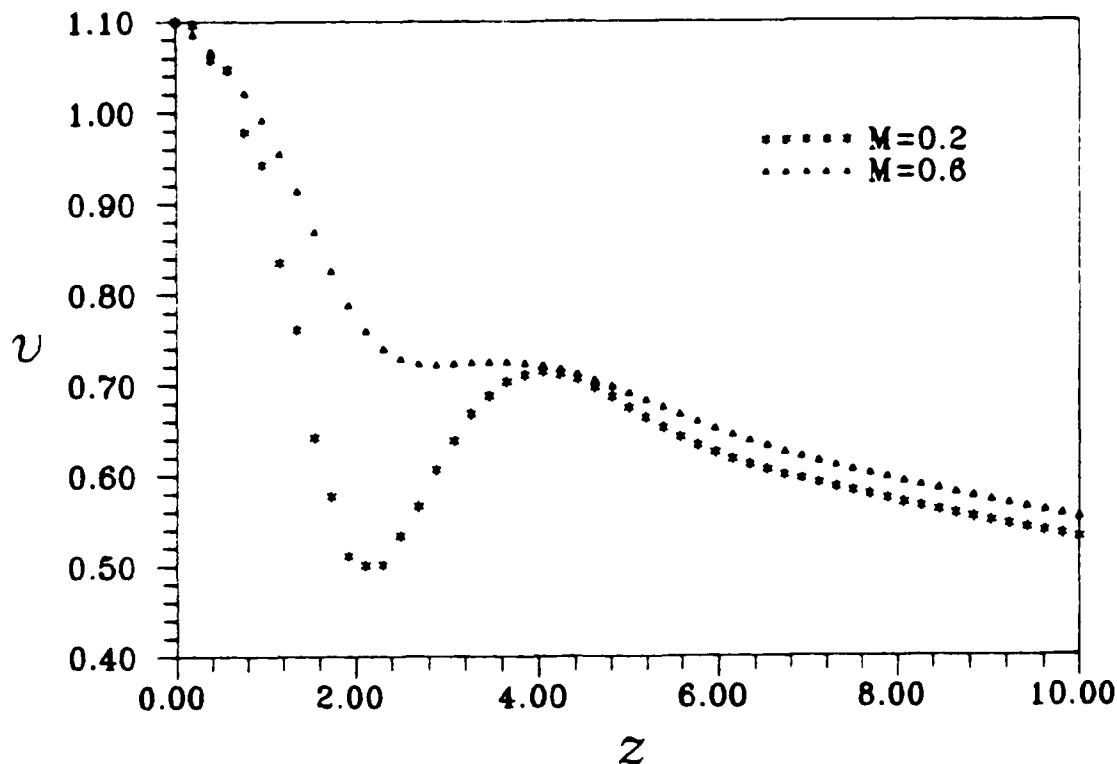


Figure 4.9. v profiles on the centerline for various Mach numbers, $Re = 200$ and $V = 1.0$

$M = 0.5$. Thus, by increasing Mach number, breakdown is effectively delayed for V held constant.

To explain this trend a look at the relevant terms in the radial momentum equation proves fruitful. Beran (2) found that with the assumption of a quasi-cylindrical flow, the relevant terms in the incompressible flow radial momentum equation are

$$\frac{v^2}{r} \approx \frac{\partial p}{\partial r} \quad (4.1)$$

Similarly for compressible flow, the radial momentum equation becomes

$$\frac{\rho v^2}{r} \approx \frac{\partial p}{\partial r} \quad (4.2)$$

The assumption of quasi-cylindrical flow is not a perfect assumption but certainly retains the largest terms of the radial momentum equation and becomes more applicable as M gets larger, as can be observed in Figure 4.7. Integrating equation 4.2 with respect to r

across the domain obtains the relationship

$$p_\infty - p_o = \int_o^R \frac{\rho v^2}{r} dr, \quad (4.3)$$

but p_∞ is equal to zero if R is large enough. So, equation 4.3 becomes

$$p_o = - \int_o^R \frac{\rho v^2}{r} dr. \quad (4.4)$$

To obtain the axial pressure gradient on the centerline, take the partial derivative of equation 4.4 with respect to z , obtaining

$$\frac{\partial p_o}{\partial z} = - \int_o^R \frac{1}{r} \left(v^2 \frac{\partial \rho}{\partial z} + 2\rho v \frac{\partial v}{\partial z} \right) dr. \quad (4.5)$$

Beran (2) found that for z between the inflow and the axial position of minimum axial velocity, an adverse pressure gradient caused a stagnation of the flow. The terms $\frac{1}{r}$, v^2 , and $2\rho v$ are positive definite, so the terms $\frac{\partial \rho}{\partial z}$ and $\frac{\partial v}{\partial z}$ become the terms that can cause a favorable pressure gradient or an adverse pressure gradient for a compressible flow. Figure 4.9 shows the axial profiles of v at $R = 1$ and for $M = 0.2$ and 0.4 . Both the $M = 0.2$ and 0.4 profiles have a negative $\frac{\partial v}{\partial z}$, with its magnitude getting smaller as M is increased. The second part of equation 4.5 then provides an adverse pressure gradient whose magnitude gets smaller as M is increased. The axial density profiles in figure 4.8 provide information on the first term in equation 4.5. The term $\frac{\partial \rho}{\partial z}$ is positive and gets larger as M is increased. This again decays the adverse pressure gradient by providing a negative $\frac{\partial p}{\partial z}$ contribution. In summary, as M is increased the adverse pressure gradient, by which the axial velocity on the centerline is stagnated, is reduced.

It is also interesting to note that as M is increased at regular intervals the density profiles change in like manner. This relationship explains the near linear behavior of Figure 4.6. A solution was obtained at $M = 1.0$ without difficulty, even though the non-conservative form of the equations was used. No spikes in the velocity profiles were observed. The flow solution is composed of weak shock waves. The assumption of a linear

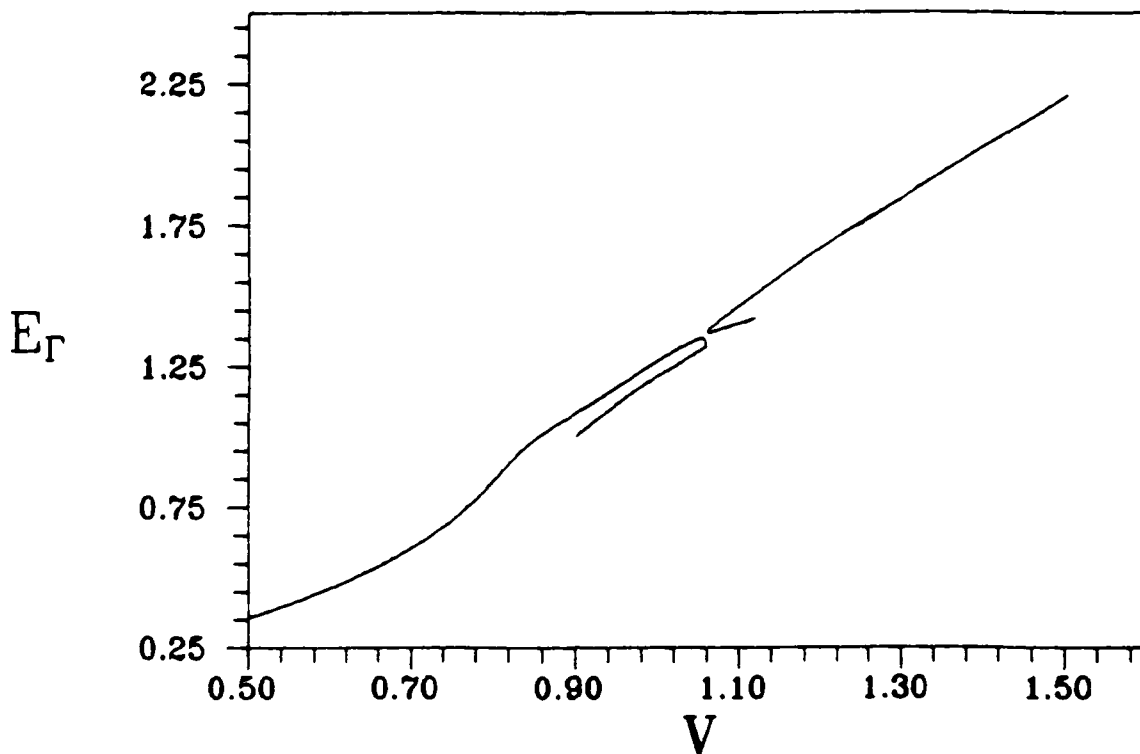


Figure 4.10. Continuation in V for $Re = 200$ and $M = 0.2$

viscosity temperature relationship produces a maximum error of 5.0% at this Mach number however.

4.4 *V* Continuation at Various Mach Numbers

One of the important discoveries of Beran (2) was the existence of non-unique solutions for a range of vortex strengths and $Re = 200$. One of the objectives of this work is to see what happens to the non-unique solutions as Mach number is increased. An important first step is to reproduce the non-unique behavior as $M \rightarrow 0$.

Figure 4.10 shows a continuation run at $M = 0.2$, $Re = 200$, and $0.5 \leq V \leq 3.0$. The non-unique behavior does indeed exist at this low Mach number. A change in sign of the Jacobian matrix determinant was found at the limit point, which generally is associated with a change in stability. At $V = 0.9$, the continuation process broke down. This was probably due to a second limit point with too large a value of d to resolve. In an attempt to fill in this curve the $M = 0.4$ and $V = 1.5$ solution was used to obtain an $M = 0.2$

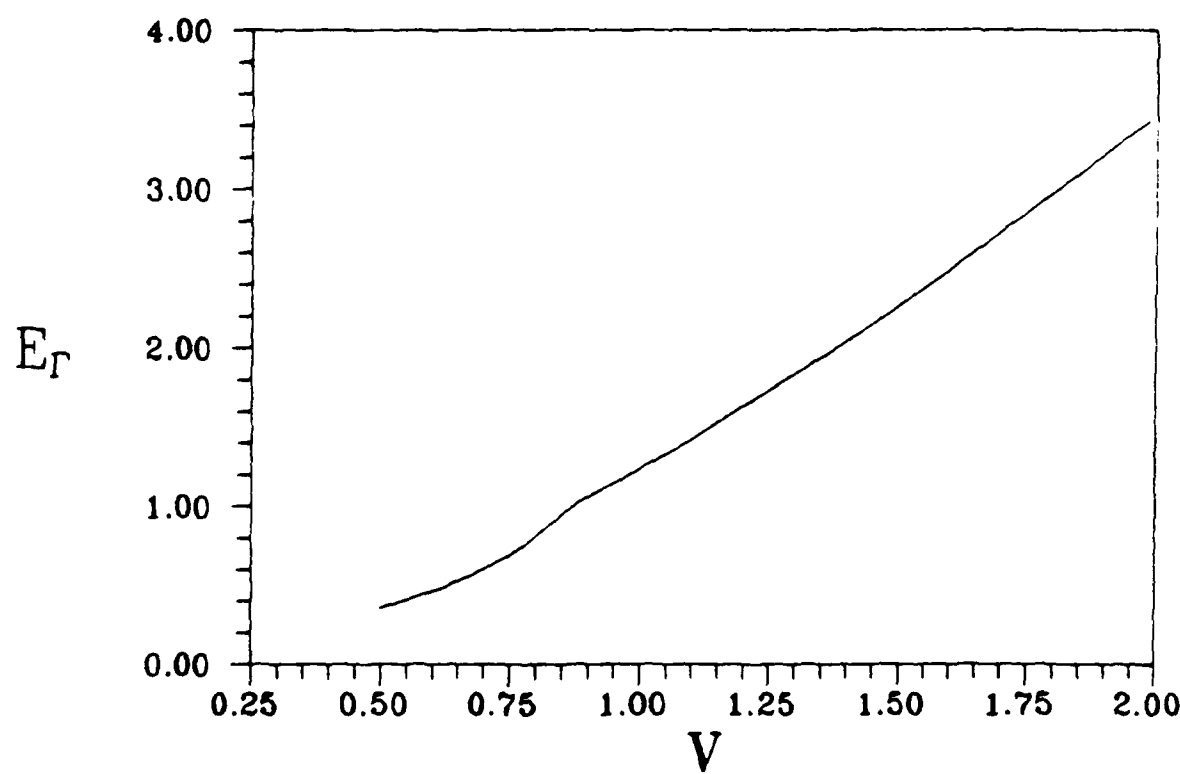


Figure 4.11. Continuation in V for $Re = 200$ and $M = 0.4$

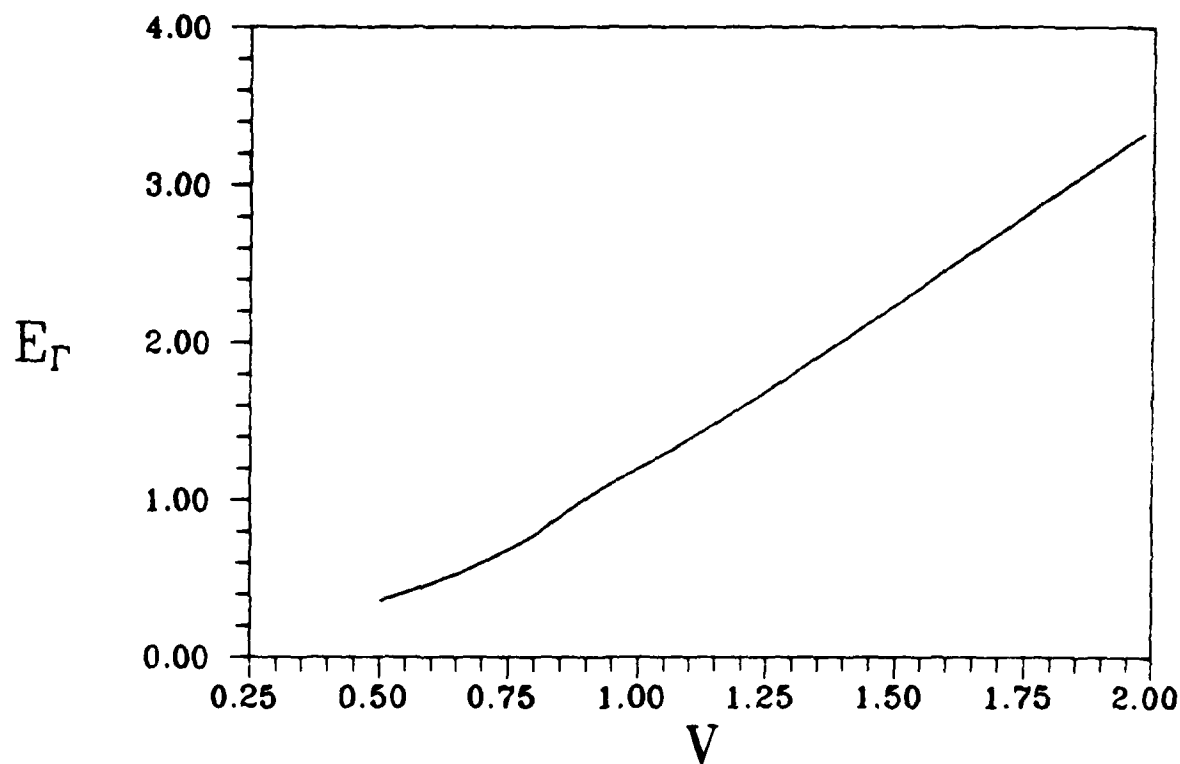


Figure 4.12. Continuation in V for $Re = 200$ and $M = 0.6$

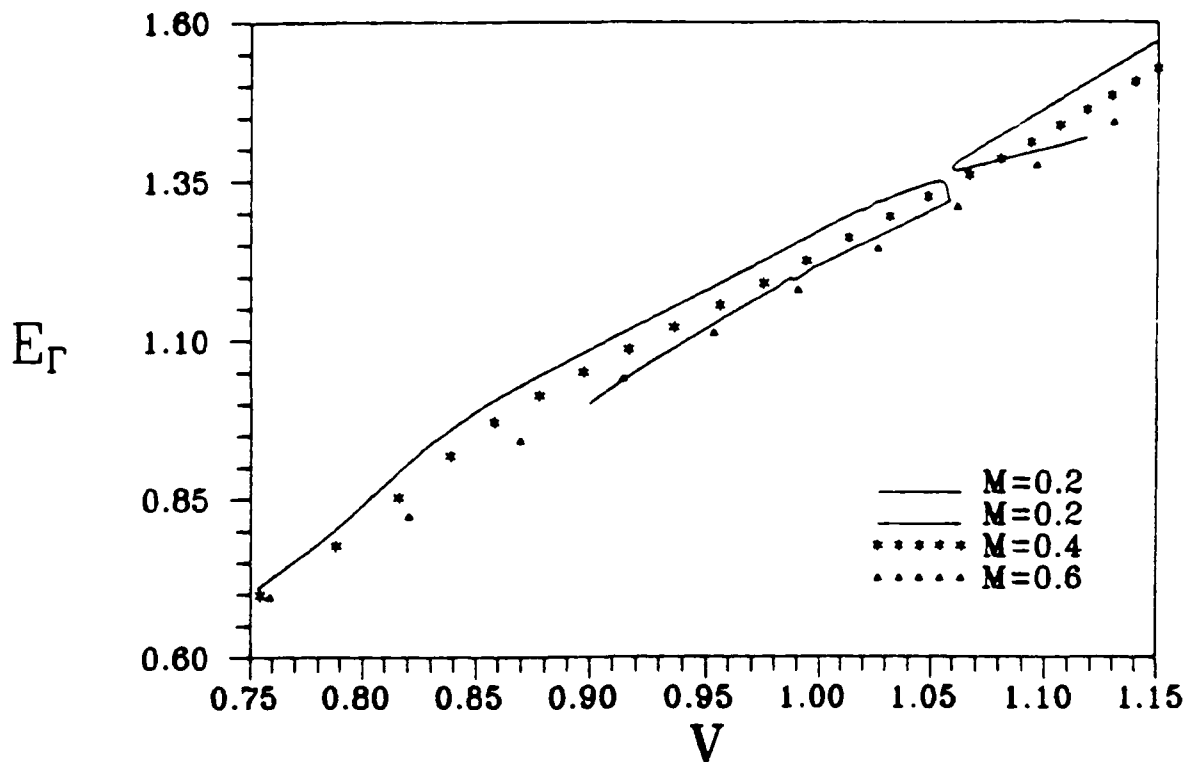


Figure 4.13. Continuation in V for $Re = 200$ and $M = 0.2, 0.4$, and 0.6

and $V = 1.5$ solution through continuation in M . This solution was then used to begin a continuation run down from $V = 1.5$. Another limit point was found near the previous one at $V = 1.0589$. The sign of the determinant changed through the second limit point. The curves were not able to be connected because of the breakdown of the continuation process. Continuation runs were then made for $M = 0.4$ and $M = 0.6$. These curves are shown in Figures 4.11 and 4.12. Non-unique solutions were not evident in these runs, and no change in sign of the determinant was found. Both solution paths were taken to extremely high vortex strengths to ensure the absence of non-unique solutions.

Figure 4.13 is a composite plot of the three continuation runs in the region of non-unique solutions. The three solutions are practically coincidental up to a vortex strength of approximately 0.75. At $V = 0.75$ the three curves separate. The $M = 0.2$ path makes an abrupt slope change and then runs a parallel course with the other two solution paths until $V = 1.0587$. At $V = 1.0587$ a limit point is encountered. The $M = 0.4$ solution exhibits some of the slope change at $V = 0.75$ as well, but not as abrupt a change for

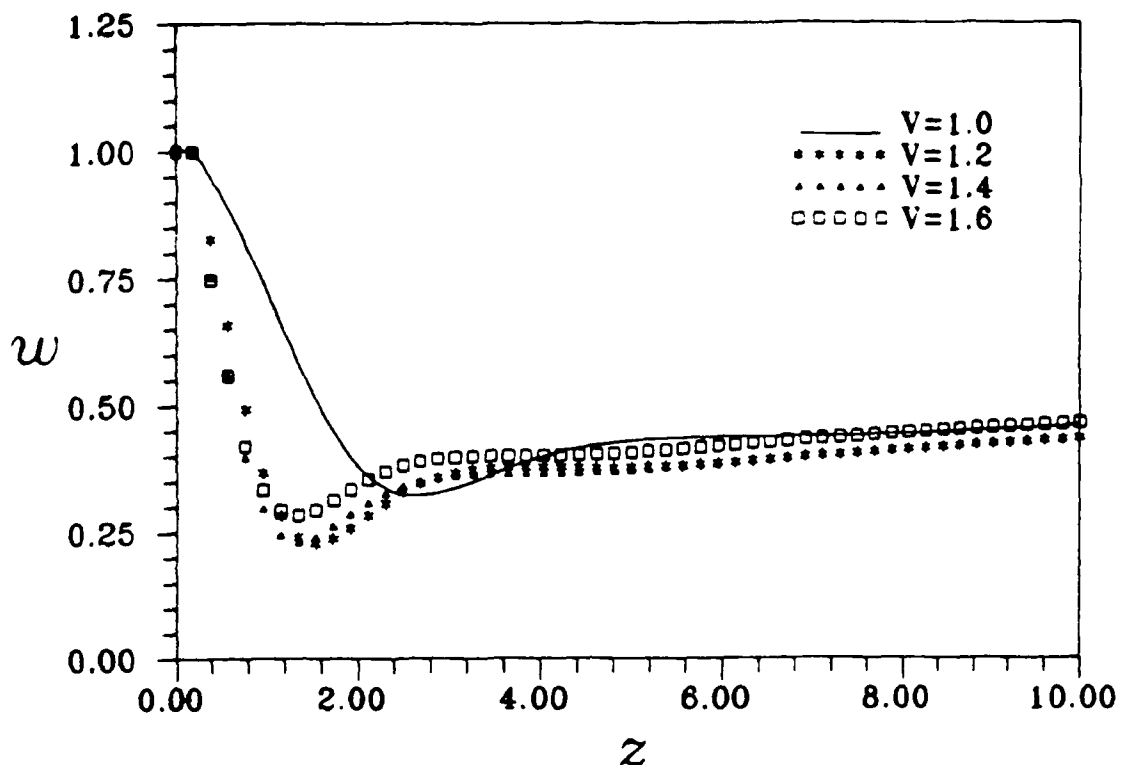


Figure 4.14. w profiles on the centerline for various V 's at $Re = 200$ and $M = 0.8$

$M = 0.2$. The $M = 0.6$ curve makes an even smaller slope change and then runs a parallel course to the $M = 0.4$ path.

Figures 4.14 and 4.15 show the centerline axial velocity and density profiles of four increasing vortex strengths at $M = 0.8$. These solutions are presented to show the effects of increasing V at a high Mach number. As V was increased the minimum value of w moves towards the inflow boundary until a certain value of V is reached. For $M = 0.8$ this value is between 1.0 and 1.2. At this point increasing V compresses the fluid on the centerline with slight increases in the minimum w . This increase in minimum w was due to an enforcement of conservation of mass as density becomes lower at this axial position. There was no reverse flow observed for this Mach number.

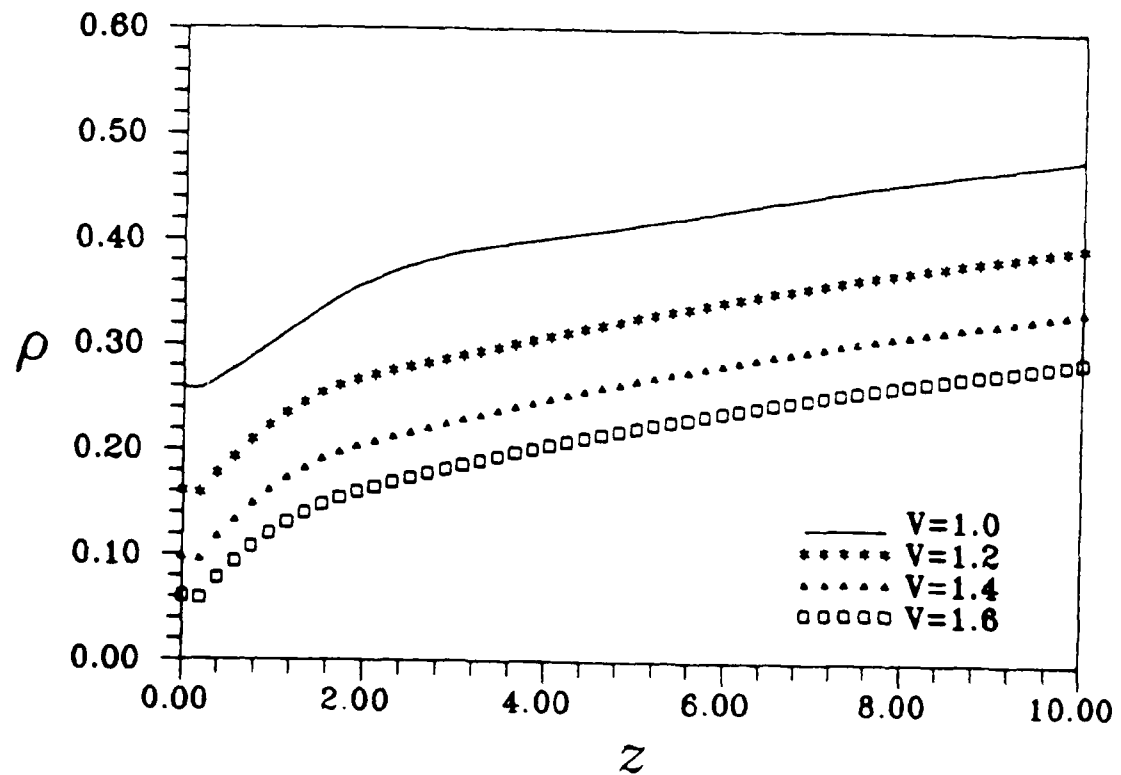


Figure 4.15. ρ profiles on the centerline for various V 's at $Re = 200$ and $M = 0.8$

V. Conclusions and Recommendations

This chapter discusses the results presented in Chapter 4 and the difficulties encountered in finding the proper boundary conditions. A summary of the effects of compressibility on the vortex breakdown and a presentation of recommendations for follow on study are given.

5.1 Solution Sensitivity to Boundary Conditions

Determining the boundary conditions for the compressible vortex was not a trivial task. Unlike many fluid dynamics problems, the inflow conditions are at a station where flow conditions are not necessarily known. The conditions on u , v , and w were taken from Beran's incompressible study (2). Conditions that specify the inflow density and internal energy profiles become very difficult to obtain. The first set of conditions tried were columnar flow conditions, $\rho_z = w_z = e_z = 0$. Since the typical solution to the incompressible flow equations is damped oscillatory motion, specification of a *locally* columnar flow should have set the conditions at the peak of one of the flow oscillations. The result of these conditions was immediate divergence even at very low values of V . This suggests an overconstraint in the conditions.

To alleviate this problem, the conditions on ρ and e were changed. A density profile was obtained by solving the columnar flow equations and used as a Dirichlet condition on ρ . Then the u momentum equation was evaluated on the inflow boundary with axial derivatives approximated by first-order difference operators. This was necessary since second-order operators would increase the bandwidth by 5, which was unacceptable computationally. These conditions worked for lower values of V , but at $V = 0.8$, large-amplitude numerical noise appeared at the inflow boundary and grew worse as V was increased. Satisfying the u momentum equation at the inflow boundary as the condition on ρ , and satisfying the v momentum equation as the condition on e , was also tried with similar results.

It seemed as though the lack of information on e was causing the difficulty, so the next set of conditions tried were conditions on ρ , u , v , and w alone, allowing e to be

set by the governing equations. Specifically, these conditions were $\rho = \rho_0$ obtained from the columnar flow equations, $u = 0$, v set by Figure 2.2, $w = 1$, and $w_z = 0$. These conditions worked well for $Re = 200$ and the range of V 's physically attainable and were the conditions used throughout this work. The iterative solution process diverges for higher Reynolds numbers due to the boundary conditions though, hence the reason $Re = 200$ was used throughout the study. A more robust set of conditions need to be determined. Either experimental ρ and ϵ profiles, or an extension of the quasi-cylindrical equations found in Beran (2) to compressible flow should be utilized. In the absence of vortex breakdown, the quasi-cylindrical equations approximate trailing vortices at high Reynolds numbers very well. For this reason, they should provide a good set of initial conditions for ρ or ϵ .

5.2 Compressibility Trends

There were some very interesting trends observed in this compressibility study. Compressibility has a favorable effect, from the viewpoint of an aerodynamicist, on vortex breakdown. This can be observed in Section 4.3; as Mach number was increased, breakdown was quickly lost. This was probably due to compression of the fluid reducing the adverse pressure gradient on the centerline, destroying the the vortex breakdown phenomenon.

In Section 4.4, the effect of varying vortex strength for a constant Re and M was analyzed. When flow solutions at $M = 0.8$ were computed, reversed flow was not observed, even for extremely large values of V .

Beran's incompressible study (2) showed the occurrence of non-unique solutions for increasing V at $Re = 200$, and at realistic vortex strengths. As Mach number was increased, these non-unique solutions disappeared. This is desirable because multiple solutions cause problems with time-integration schemes, since the observed steady state solution becomes dependent on the initial flow state.

In summary, as Mach number was increased for $Re = 200$ and $V = 1.0$, breakdown was lost at about $M = 0.5$. As vortex strength was increased for $M = 0.8$, the minimum value of w moved towards the inflow boundary, as was reported by Beran (2). In Beran's incompressible study (2) as V was increased other local minima were observed. In the

compressible study, when V grew large enough the minimum w stopped moving toward the inflow, but instead of producing more local minima as in incompressible flow, the fluid becomes more compressed.

5.3 Recommendations for Follow-on Study

During the course of this study original goals of mapping out the solution space for various values of Re , V , and M had to be reduced to accomplishing a compressibility study at low Reynolds number for various vortex strengths. This was due to time constraints and the difficulties encountered with the boundary conditions. One can see that a logical follow-on study would be to derive a set of robust boundary conditions that can accommodate larger Reynolds numbers, as well as various Mach numbers and vortex strengths. This follow-on study would benefit time integration studies as well, since time-integration codes may converge on a solution even if the wrong set of boundary conditions are used. The compressible quasi-cylindrical equations mentioned previously are a promising starting point.

Once these boundary conditions are determined, simulations at higher Reynolds numbers should be run to determine whether non-unique solutions can be found. Also, flow structures should be studied to determine if the same trends are found for high Reynolds numbers as was found for $Re = 200$.

Finally, a compressible time-integration code should be developed to determine the stability of the different branches in the continuation curves. With the current study and the follow on topics providing the compressible flow information on vortex breakdown, one would hope that future investigators would be able to put the experimental, analytical, and numerical studies together to form a better understanding of the vortex breakdown problem.

Appendix A. Derivation of the Governing Equations

The derivation of the governing equations was performed by utilizing the nondimensional general curvilinear coordinate Navier Stokes equations found in reference (34). The general continuity equation is:

$$\frac{\partial \rho}{\partial t} + \frac{1}{h_1 h_2 h_3} \frac{\partial}{\partial x_j} \left(\frac{1}{h_j} h_1 h_2 h_3 \rho u_j \right) = 0 \quad (A.1)$$

where the j subscript denotes summation. Cylindrical coordinates were used in the model. In cylindrical coordinates $x_1 = r$, $x_2 = \theta$, and $x_3 = z$ with velocity components u_j equal to u , v , and w . The metrics h_j are as follows: $h_1 = 1$, $h_2 = r$, and $h_3 = 1$. Equation A.1 becomes:

$$\frac{\partial \rho}{\partial t} + \frac{1}{r} \left[\frac{\partial}{\partial r} (r \rho u) + \frac{\partial}{\partial \theta} (\rho v) + \frac{\partial}{\partial z} (r \rho w) \right] = 0 \quad (A.2)$$

Two of the main assumptions of this thesis are $\frac{\partial \rho}{\partial t} = 0$ (steady state) and $\frac{\partial \rho}{\partial \theta} = 0$ (axisymmetric). With these assumptions applied to Equation A.2 the cylindrical axisymmetric continuity equation becomes:

$$\frac{\partial}{\partial r} (\rho u) + \frac{\rho u}{r} + \frac{\partial}{\partial z} (\rho w) = 0 \quad (A.3)$$

The general curvilinear coordinate momentum equation in the x_1 direction can be written:

$$\begin{aligned} \frac{\partial}{\partial t} (\rho u_1) + \frac{1}{h_1 h_2 h_3} \frac{\partial}{\partial x_j} \left(\frac{1}{h_j} h_1 h_2 h_3 \mathcal{F}_{j1} \right) + \frac{1}{h_1 h_2} \left(\mathcal{F}_{12} \frac{\partial h_1}{\partial x_2} - \mathcal{F}_{22} \frac{\partial h_1}{\partial x_1} \right) \\ + \frac{1}{h_1 h_3} \left(\mathcal{F}_{13} \frac{\partial h_1}{\partial x_3} - \mathcal{F}_{33} \frac{\partial h_1}{\partial x_1} \right) = 0 \end{aligned} \quad (A.4)$$

with the other two momentum equations following by cyclic permutation and where \mathcal{F}_{ij} are the components of the tensor \mathcal{F} :

$$\mathcal{F}_{ij} = \rho u_i u_j + p \delta_{ij} - \frac{1}{Re} \tau_{ij} \quad (A.5)$$

τ_{ij} is the stress tensor and is defined:

$$\tau_{ij} = -\frac{2}{3}\mu(\nabla \cdot V)\delta_{ij} + 2\mu(defV)_{ij} \quad (A.6)$$

and δ_{ij} is the Kronecker delta.

$$\nabla \cdot V = \frac{1}{h_1 h_2 h_3} \frac{\partial}{\partial x_i} \left(\frac{1}{h_i} h_1 h_2 h_3 u_i \right) \quad (A.7)$$

$$(defV)_{11} = \frac{1}{h_1} \left(\frac{\partial u_1}{\partial x_1} + \frac{u_2}{h_2} \frac{\partial h_1}{\partial x_2} + \frac{u_3}{h_3} \frac{\partial h_1}{\partial x_3} \right) \quad (A.8)$$

with $(defV)_{22}$ and $(defV)_{33}$ following by cyclic permutation.

$$(defV)_{ij(i \neq j)} = \frac{1}{2} \left[\frac{1}{h_i} \frac{\partial u_j}{\partial x_i} + \frac{1}{h_j} \frac{\partial u_i}{\partial x_j} - \frac{1}{h_i h_j} \left(u_i \frac{\partial h_i}{\partial x_j} + u_j \frac{\partial h_j}{\partial x_i} \right) \right] \quad (A.9)$$

Now using the specific coordinates and metrics defined in the derivation of the continuity equation above and remembering $\frac{\partial(\cdot)}{\partial \theta} = 0$ these definitions become:

$$\nabla \cdot V = \frac{1}{r} \left[\frac{\partial}{\partial r} (ru) + \frac{\partial}{\partial \theta} (v) + \frac{\partial}{\partial z} (rw) \right] = u_r + \frac{u}{r} + w_z \quad (A.10)$$

$$(defV)_{11} = u_r \quad (A.11)$$

$$(defV)_{22} = \frac{u}{r} \quad (A.12)$$

$$(defV)_{33} = w_z \quad (A.13)$$

$$(defV)_{31} = \frac{1}{2} \left(\frac{\partial u}{\partial z} + \frac{\partial w}{\partial r} \right) = \frac{1}{2} (u_z + w_r) \quad (A.14)$$

$$\tau_{31} = 2\mu \left[\frac{1}{2} (u_z + w_r) \right] = \mu (u_z + w_r) \quad (A.15)$$

$$\tau_{11} = -\frac{2}{3}\mu \left(u_r + \frac{u}{r} + w_z \right) + 2\mu u_r \quad (A.16)$$

$$\tau_{22} = -\frac{2}{3}\mu \left(u_r + \frac{u}{r} + w_z \right) + 2\mu \frac{u}{r} \quad (A.17)$$

After making the assumption of steady state and axisymmetry Equation A.4 becomes:

$$\frac{1}{r} \frac{\partial}{\partial r} (r \mathcal{F}_{11}) + \frac{1}{r} \frac{\partial}{\partial z} (r \mathcal{F}_{31}) - \frac{\mathcal{F}_{22}}{r} = 0 \quad (\text{A.18})$$

using the relationships A.10- A.17 the relevant \mathcal{F} terms become:

$$\mathcal{F}_{11} = \rho uu + p - \frac{1}{Re} \left[-\frac{2}{3} \mu \left(u_r + \frac{u}{r} + w_z \right) + 2\mu u_r \right] \quad (\text{A.19})$$

$$\mathcal{F}_{31} = \rho uw - \frac{1}{Re} [\mu (u_z + w_r)] \quad (\text{A.20})$$

$$\mathcal{F}_{22} = \rho vv + p - \frac{1}{Re} \left[-\frac{2}{3} \mu \left(u_r + \frac{u}{r} + w_z \right) + 2\mu \frac{u}{r} \right] \quad (\text{A.21})$$

Substituting these terms into A.18 the u momentum equation becomes:

$$\begin{aligned} \frac{\partial}{\partial r} \left[\rho uu + p - \frac{1}{Re} \left(\frac{4}{3} \mu u_r - \frac{2}{3} \mu \frac{u}{r} - \frac{2}{3} \mu w_z \right) \right] + \frac{1}{r} \left[\rho uu + p - \frac{1}{Re} \left(\frac{4}{3} \mu u_r - \frac{2}{3} \mu \frac{u}{r} - \frac{2}{3} \mu w_z \right) \right] \\ + \frac{\partial}{\partial z} \left[\rho uw - \frac{1}{Re} \mu (u_z + w_r) \right] - \frac{1}{r} \left[\rho vv + p - \frac{1}{Re} \left(-\frac{2}{3} \mu u_r + \frac{4}{3} \mu \frac{u}{r} - \frac{2}{3} \mu w_z \right) \right] = 0 \end{aligned}$$

Subtracting continuity and combining terms:

$$\begin{aligned} \rho uu_r - \frac{\rho v^2}{r} + \rho w u_z + p_r = \\ \frac{1}{Re} [\mu_r (4/3 u_r - 2/3 \frac{u}{r} - 2/3 w_z) + \mu_z (u_z + w_r)] \\ + \mu (4/3 u_{rr} + 4/3 \frac{u_r}{r} - 4/3 \frac{u}{r^2} + u_{zz} + 1/3 w_{rz}) \end{aligned} \quad (\text{A.22})$$

In Section 2.1 the equation of state was given to relate p , ρ , and ϵ :

$$p = (\gamma - 1) \rho \epsilon \quad (\text{A.23})$$

The linearized viscosity-temperature relationship was also given to relate μ and ϵ :

$$\mu = c_1 \epsilon + c_2 \quad (\text{A.24})$$

where c_1 and c_2 are defined by Equations 2.16 and 2.17. Substituting these relationships

into A.23 the u momentum equation is obtained:

$$\begin{aligned} \rho u u_r - \frac{\rho v^2}{r} + \rho w u_z + (\gamma - 1)(\rho \epsilon)_r = \\ \frac{1}{R \epsilon} [c_1 \epsilon_r (4/3 u_r - 2/3 \frac{u}{r} - 2/3 w_z) + c_1 \epsilon_z (u_z + w_r)] \\ + (c_1 \epsilon + c_2) (4/3 u_{rr} + 4/3 \frac{u_r}{r} - 4/3 \frac{u}{r^2} + u_{zz} + 1/3 w_{rz}) \end{aligned} \quad (A.25)$$

The v momentum equation found by cyclic permutation and the application of previously mentioned assumptions is:

$$\frac{1}{r} \frac{\partial}{\partial r} (r \mathcal{F}_{12}) + \frac{1}{r} \frac{\partial}{\partial z} (r \mathcal{F}_{32}) + \frac{\mathcal{F}_{21}}{r} = 0 \quad (A.26)$$

For the v momentum equation more of the $(defV)_{ij}$ and τ_{ij} terms must be defined:

$$(defV)_{12} = (defV)_{21} = \frac{1}{2} \left(v_r - \frac{v}{r} \right) \quad (A.27)$$

$$(defV)_{32} = \frac{1}{2} (v_z) \quad (A.28)$$

$$\tau_{12} = \tau_{21} = \mu \left(v_r - \frac{v}{r} \right) \quad (A.29)$$

$$\tau_{32} = \mu (v_z) \quad (A.30)$$

Using A.27- A.30 the relevant \mathcal{F}_{ij} terms become:

$$\mathcal{F}_{12} = \mathcal{F}_{21} = \rho u v - \frac{1}{R \epsilon} \left[\mu \left(v_r - \frac{v}{r} \right) \right] \quad (A.31)$$

$$\mathcal{F}_{32} = \rho v w - \frac{1}{R \epsilon} [\mu (v_z)] \quad (A.32)$$

Substituting these terms into A.26 the equation becomes:

$$\begin{aligned} \frac{\partial}{\partial r} \left[\rho u v - \frac{1}{R \epsilon} \left(\frac{4}{3} \mu v_r - \mu \frac{v}{r} \right) \right] + \frac{1}{r} \left[\rho u v - \frac{1}{R \epsilon} \left(\mu v_r - \mu \frac{v}{r} \right) \right] \\ + \frac{\partial}{\partial z} \left[\rho v w - \frac{1}{R \epsilon} \mu (v_z) \right] + \frac{1}{r} \left[\rho u v - \frac{1}{R \epsilon} \left(\mu v_r + \mu \frac{v}{r} \right) \right] = 0 \end{aligned}$$

Subtracting continuity and combining terms:

$$\begin{aligned} \rho u v_r + \frac{\rho u v}{r} + \rho w v_z = \\ \frac{1}{R \epsilon} [\mu_r (v_r - \frac{v}{r}) + \mu_z (v_z) \\ + \mu (v_{rr} + \frac{v_r}{r} - \frac{v}{r^2} + v_{zz})] \end{aligned} \quad (A.33)$$

Using Equation A.24 the v momentum equation becomes:

$$\begin{aligned} \rho u v_r + \frac{\rho u v}{r} + \rho w v_z = \\ \frac{1}{R \epsilon} [c_1 \epsilon_r (v_r - \frac{v}{r}) + c_1 \epsilon_z (v_z) \\ + (c_1 \epsilon + c_2) (v_{rr} + \frac{v_r}{r} - \frac{v}{r^2} + v_{zz})] \end{aligned} \quad (A.34)$$

The w momentum equation found by cyclic permutation and the application of previously mentioned assumptions is:

$$\frac{1}{r} \frac{\partial}{\partial r} (r \mathcal{F}_{13}) + \frac{1}{r} \frac{\partial}{\partial z} (r \mathcal{F}_{33}) = 0 \quad (A.35)$$

For the w momentum equation more of the $(defV)_{ij}$ and τ_{ij} terms must be defined:

$$(defV)_{13} = \frac{1}{2} (w_r + u_z) \quad (A.36)$$

$$\tau_{13} = \mu (w_r + u_z) \quad (A.37)$$

$$\tau_{33} = \mu \left(-\frac{2}{3} u_r - \frac{2}{3} \frac{u}{r} + \frac{4}{3} w_z \right) \quad (A.38)$$

Using A.36- A.38 the relevant \mathcal{F}_{ij} terms become:

$$\mathcal{F}_{13} = \rho u w - \frac{1}{R \epsilon} [\mu (w_r + u_z)] \quad (A.39)$$

$$\mathcal{F}_{33} = \rho w w + p - \frac{1}{R \epsilon} \left[\mu \left(-\frac{2}{3} u_r - \frac{2}{3} \frac{u}{r} + \frac{4}{3} w_z \right) \right] \quad (A.40)$$

Substituting these terms into A.35 the equation becomes:

$$\begin{aligned} \frac{\partial}{\partial r} \left[\rho u w - \frac{1}{Re} (\mu u_r + \mu u_z) \right] + \frac{1}{r} \left[\rho u w - \frac{1}{Re} (\mu u_r + \mu u_r) \right] \\ + \frac{\partial}{\partial z} \left[\rho u w - \frac{1}{Re} \left(-\frac{2}{3} \mu u_r - \frac{2}{3} \mu \frac{u}{r} + \frac{4}{3} \mu u_z \right) \right] = 0 \end{aligned}$$

Subtracting continuity and combining terms:

$$\begin{aligned} \rho u w_r + \rho w w_z + p_z = \\ \frac{1}{Re} [\mu_r (w_r + u_z) + \mu_z (-2/3 u_r - 2/3 \frac{u}{r} + 4/3 w_z)] \\ + \mu (1/3 u_{rz} + 1/3 \frac{u_z}{r} + w_{rr} + \frac{w_r}{r} + 4/3 w_{zz}) \end{aligned} \quad (A.41)$$

Using Equation A.24 the w momentum equation becomes:

$$\begin{aligned} \rho u w_r + \rho w w_z + (\gamma - 1)(\rho e)_z = \\ \frac{1}{Re} [c_1 e_r (w_r + u_z) + c_1 e_z (-2/3 u_r - 2/3 \frac{u}{r} + 4/3 w_z)] \\ + (c_1 e + c_2) (1/3 u_{rz} + 1/3 \frac{u_z}{r} + w_{rr} + \frac{w_r}{r} + 4/3 w_{zz}) \end{aligned} \quad (A.42)$$

The non-dimensional general curvilinear coordinate energy equation can be written:

$$\frac{\partial}{\partial t} (\rho E) + \frac{1}{h_1 h_2 h_3} \frac{\partial}{\partial z_j} \left\{ \frac{1}{h_j} h_1 h_2 h_3 \left[(\rho E + p) u_j - \frac{1}{Re} \tau_{j1} u_1 - \frac{\gamma k}{Re Pr} \frac{1}{h_j} \frac{\partial e}{\partial z_j} \right] \right\} = 0 \quad (A.43)$$

where $E = e + \frac{1}{2}(u^2 + v^2 + w^2)$. Now applying the above assumptions and metrics A.43 becomes:

$$\begin{aligned} \frac{\partial}{\partial r} \left[\rho u \epsilon + \frac{1}{2} (\rho u^3 + \rho u v^2 + \rho u w^2) + p u - \frac{1}{Re} (\tau_{11} u \tau_{12} v + \tau_{13} w) - \frac{\gamma k}{Re Pr} \frac{\partial \epsilon}{\partial r} \right] \\ + \frac{\partial}{\partial z} \left[\rho \epsilon w + \frac{1}{2} (\rho u^2 w + \rho v^2 w + \rho w^3) + p w - \frac{1}{Re} (\tau_{31} u + \tau_{32} v + \tau_{33} w) - \frac{\gamma k}{Re Pr} \frac{\partial \epsilon}{\partial z} \right] = 0 \end{aligned} \quad (A.44)$$

The stress tensor terms in Equation A.45 have all been defined above. Applying these terms and using A.23 A.45 becomes:

$$\begin{aligned}
& \gamma \left[\frac{\rho u \epsilon}{r} + (\rho u \epsilon)_r + (\rho w \epsilon)_z \right] + \frac{\rho_r}{2} [u^3 + uv^2 + uw^2] + \frac{\rho_z}{2} [u^2 w + v^2 w + w^3] \\
& + \frac{\rho}{2} [(u^3)_r + (uv^2)_r + (uw^2)_r + (u^2 w)_z + (v^2 w)_z + (w^3)_z + \frac{u^3}{r} + \frac{uv^2}{r} + \frac{uw^2}{r}] = \\
& \frac{1}{Re} [c_1 \epsilon_r (4/3 u u_r - 2/3 \frac{u^2}{r} - 2/3 u w_z + v v_r - \frac{v^2}{r} + u_z w + u w_r) \\
& + c_1 \epsilon_z (u u_z + u w_r + v v_z - 2/3 u_r w - 2/3 \frac{u w}{r} + 4/3 u w_z) \quad (A.45) \\
& + (c_1 \epsilon + c_2) (4/3 u_r^2 + 4/3 u u_{rr} - 4/3 u_r w_z + 1/3 u w_{rz} + 1/3 u_{rz} w + v_r^2 \\
& + v v_{rr} - \frac{v v_r}{r} + 2 u_z w_r + w_r^2 + w w_{rr} + u_z^2 + u u_{zz} + v_z^2 + v v_{zz} \\
& + 1/3 \frac{u_z w}{r} - 4/3 \frac{u w_z}{r} + 4/3 w_z^2 + 4/3 w w_{zz} - 2/3 \frac{u^2}{r} - \frac{v^2}{r} + \frac{w w_r}{r}) \\
& + \frac{\gamma}{Pr} \left[(c_1 \epsilon + c_2) (\epsilon_{rr} + \epsilon_{zz} + \frac{e_r}{r}) + c_1 \epsilon_r^2 + c_1^2 \right]]
\end{aligned}$$

Appendix B. Derivation of Representative Analytic Jacobian Elements

The purpose of this appendix is to set up Newton's method for a representative equation. The process of going from a differential equation to an algebraic equation and then computing the associated analytic Jacobian elements is described in detail.

Due to its simplicity the continuity equation will be used to demonstrate the process.

The differential form of the continuity equation is:

$$(\rho u)_r + \frac{\rho u}{r} + (\rho w)_z = 0 \quad (B.1)$$

The first step is to put the equation in non-conservative form:

$$\rho_r u + \rho u_r + \frac{\rho u}{r} + \rho_z w + \rho w_z = 0 \quad (B.2)$$

In the discretization process all partial derivatives in the interior equations are replaced with discrete operators. In a 2-D implicit scheme with J nodes in the r direction, I nodes in the z direction, and $J < I$ a column by column numbering system produces the smallest bandwidth of the banded system to be solved. The stencil used is found in Figure B.1. With this stencil, the second order central difference operator is:

$$\delta_z u = \frac{u_{k1} - u_{k3}}{2\Delta z} \quad (B.3)$$

Applying the δ_r and δ_z operators to each of the terms in Equation B.2 it becomes:

$$\left[\frac{\rho_{k2} - \rho_{k4}}{2\Delta r} \right] u_k + \rho_k \left[\frac{u_{k2} - u_{k4}}{2\Delta r} \right] + \frac{\rho_k u_k}{r_k} + \left[\frac{\rho_{k1} - \rho_{k3}}{2\Delta z} \right] w_k + \rho_k \left[\frac{u_{k1} - u_{k3}}{2\Delta z} \right] = 0 \quad (B.4)$$

This is the non-linear algebraic continuity equation to be solved by Newton's method and will be referred to as F .

The next step is to compute the analytic Jacobian elements of B.4. This is done by taking partial derivatives of B.4 with respect to each variable at each node. The Jacobian

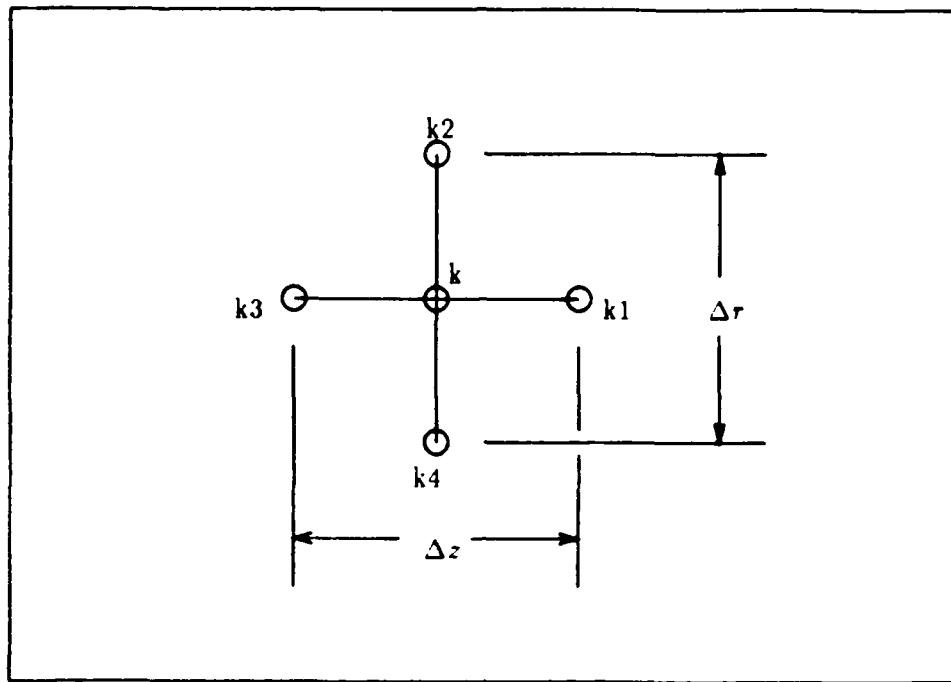


Figure B.1. Stencil used for discretization of the Continuity equation

elements associated with ρ are:

$$\frac{\partial F}{\partial \rho_k} = \left[\frac{u_{k2} - u_{k4}}{2\Delta r} \right] + \frac{u_k}{r_k} + \left[\frac{w_{k1} - w_{k3}}{2\Delta z} \right] \quad (B.5)$$

$$\frac{\partial F}{\partial \rho_{k2}} = \frac{1}{2\Delta r} u_k \quad (B.6)$$

$$\frac{\partial F}{\partial \rho_{k4}} = -\frac{1}{2\Delta r} u_k \quad (B.7)$$

$$\frac{\partial F}{\partial \rho_{k1}} = \frac{1}{2\Delta z} w_k \quad (B.8)$$

$$\frac{\partial F}{\partial \rho_{k3}} = -\frac{1}{2\Delta z} w_k \quad (B.9)$$

the elements associated with u are:

$$\frac{\partial F}{\partial u_k} = \left[\frac{\rho_{k2} - \rho_{k4}}{2\Delta r} \right] + \frac{\rho_k}{r_k} \quad (B.10)$$

$$\frac{\partial F}{\partial u_{k2}} = \frac{1}{2\Delta r} \rho_k \quad (B.11)$$

$$\frac{\partial F}{\partial u_{k4}} = -\frac{1}{2\Delta r} \rho_k \quad (B.12)$$

and the elements associated with w are:

$$\frac{\partial F}{\partial w_{k1}} = \frac{1}{2\Delta z} \rho_k \quad (B.13)$$

$$\frac{\partial F}{\partial w_{k3}} = -\frac{1}{2\Delta z} \rho_k \quad (B.14)$$

This process is repeated for the momentum equations and the energy equation, and then Newton's method is used to solve:

$$F_x \Delta x = -F \quad (B.15)$$

where F_x is the Jacobian matrix.

Bibliography

1. Beran, P.S. 1987 Numerical Simulations of Trailing Vortex Bursting. *AIAA Paper 87-1313*.
2. Beran, P.S. 1989. An Investigation of the Bursting of Trailing Vortices Using Numerical Simulation. Ph.D. Thesis, California Institute of Technology.
3. Brown, G.L. and Lopez J.M. 1988 Axisymmetric Vortex Breakdown Part II: Physical Mechanisms. *Aero. Res. Lab. Aero. Report 174*.
4. Chorin, A.J. 1967 *J. Comp. Phys.*, **2**, 2.
5. Elle, B.J. 1960 On the Breakdown at High Incidences of the Leading E. V. on Delta Wings. *J. of the Royal Aero. Soc.*, **64**, 491.
6. Falor, J.H. and Leibovich, S. 1977 Disrupted States of Vortex Flow and Vortex Breakdown. *Physics of Fluids*, **20** (9), 1385.
7. Falor, J.H. and Leibovich, S. 1978 An Experimental Map of the Internal Structure of a Vortex Breakdown. *J. Fluid Mech.*, **86** (2), 313.
8. Garg, A.K. 1977 Oscillatory Behavior in Vortex Breakdown Flows: an Experimental Study Using a Laser Doppler Anemometer. MS Thesis, Cornell University.
9. Garg, A.K. and Leibovich, S. 1979 Spectral Characteristics of Vortex Breakdown Flowfields. *Phys. Fluids*, **22** (11), 2053.
10. Grabowski, W.J. 1972 Solutions of the Navier-Stokes Equations for Vortex Breakdown. *Berkeley Report FM-74-6*.
11. Grabowski, W.J. and Berger, S.A. 1976 Solutions of the Navier-Stokes Equations for Vortex Breakdown. *J. Fluid Mech.*, **75** (3), 525.
12. Hafez, M., Kuruviла, G. and Salas, M.D. 1986 Numerical Study of Vortex Breakdown. *AIAA Paper 86-0558*.
13. Hafez, M., Ahmad, J., Kuruviла, G. and Salas, M.D. 1987 Vortex Breakdown Simulation. *AIAA Paper 87-1343*.
14. Hall, J.L. 1985 An Introduction to Vortex Breakdown and Vortex Core Bursting. *Nat. Res. Council No. 24336*.
15. Hall, M.G. 1965 A Numerical Method for Solving the Equations for a Vortex Core. *Aero. Res. Council RM-3467*.
16. Hall, M.G. 1967 A New Approach to Vortex Breakdown. *Proc. Heat Trans. Fluid Mech. Inst.*, 319.
17. Hall, M.G. 1972 Vortex Breakdown. *Ann. Rev. of Fluid Mech.*, **4**, 195.
18. Harvey, J.K. 1962 Some Observations of the Vortex Breakdown Phenomenon. *J. Fluid Mech.*, **14**, 585.
19. Isaacson, E. and Keller, H.B. 1966 *Analysis of Numerical Methods*. John Wiley & Sons, New York.

20. Keller, H.B. 1977 Numerical Solution of Bifurcation and Nonlinear Eigenvalue Problems. *Applications of Bifurcation Theory*. Academic Press, New York, p. 359.
21. Keller, H.B. 1982 Continuation Methods in Computational Fluid Dynamics. *Numerical and Physical Aspects of Aerodynamic Flows*, (ed. T. Cebeci). Springer-Verlag, New York, p. 3.
22. Kirkpatrick, D.L.I. 1964 Experimental Investigation of the Breakdown of a Vortex in a Tube. *Aero. Res. Council CP-821*.
23. Kopecky, R.M. and Torrance K.E. 1973 Initiation and Structure of Axisymmetric Eddies in a Rotating Stream. *Computers and Fluids*, **1**, 289.
24. Krause, E., Shi, X.G. and Hartwich, P.M. 1983 Computation of Leading-Edge Vortices. *AIAA Paper 83-1907*.
25. Lambourne, N.C. and Bryer, D.W. 1961 The Bursting of Leading-edge Vortices—Some Observations and Discussions of the Phenomenon. *Aero. Res. Council RM-3282*.
26. Leibovich, S. 1978 The Structure of Vortex Breakdown. *Ann. Rev. of Fluid Mech.*, **10**, 221.
27. Leibovich, S. 1983 Vortex Stability and Breakdown. *AGARD Report CP-342*, No. 23.
28. Leibovich, S. 1984 Vortex Stability and Breakdown: Survey and Extension. *AIAA Journal*, **22** (9), 1192.
29. Lopez, J.M. 1988 Axisymmetric Vortex Breakdown Part I: Confined Swirling Flow. *Aero. Res. Lab. Aero. Report 173*.
30. Menne, S. 1988 Vortex Breakdown in an Axisymmetric Flow. *AIAA Paper 88-0506*.
31. Nakamura, Y., Leonard, A. and Spalart, P.R. 1985 Vortex Breakdown Simulation. *AIAA Paper 85-1581*.
32. Nakamura, Y., Leonard, A. and Spalart, P.R. 1986 Internal Structure of a Vortex Breakdown. *AIAA Paper 86-107*.
33. Peckham, D.H. and Atkinson, S.A. 1957 Preliminary Results of Low-Speed Wind Tunnel Tests on Gothic Wing of AR 1.0. *Aero. Res. Council CP-508*.
34. Peyret, R. and Taylor, T.D. 1983 *Computational Methods for Fluid Flow*. Springer-Verlag, New York.
35. Sarpkaya, T. 1971A On Stationary and Travelling Vortex Breakdowns. *J. Fluid Mech.*, **45** (3), 585.
36. Sarpkaya, T. 1971B Vortex Breakdown in Swirling Conical Flows. *AIAA Journal*, **9** (9), 1792.
37. Sarpkaya, T. 1974 Effect of the Adverse Pressure Gradient on Vortex Breakdown. *AIAA Journal*, **12** (9), 602.

Vita

Scott Morton was born on [REDACTED] He attended high school at Granite City High School North and graduated in June of 1982. He then went on to attend Parks Air College of St Louis University where he obtained his Bachelor of Science degree in Aerospace Engineering in December of 1985. He received his commission into the United States Air Force at this time through the ROTC program at Parks. His initial assignment in the Air Force was at the Foreign Technology Division (FTD) at Wright Patterson AFB Ohio, where he analyzed foreign ballistic missiles and space launch vehicles. After three years at FTD he attended the Air Force Institute of Technology, also at Wright Patterson, to complete a Master of Science degree in Aeronautical Engineering.

UNCLASSIFIED

SECURITY CLASSIFICATION OF THIS PAGE

REPORT DOCUMENTATION PAGE

Form Approved
OMB No. 0704-0188

1a. REPORT SECURITY CLASSIFICATION Unclassified		1b. RESTRICTIVE MARKINGS							
2a. SECURITY CLASSIFICATION AUTHORITY		3. DISTRIBUTION/AVAILABILITY OF REPORT Approved for public release; distribution unlimited							
2b. DECLASSIFICATION/DOWNGRADING SCHEDULE									
4. PERFORMING ORGANIZATION REPORT NUMBER(S) AFIT/GAE/ENY/89D-24		5. MONITORING ORGANIZATION REPORT NUMBER(S)							
6a. NAME OF PERFORMING ORGANIZATION School of Engineering	6b. OFFICE SYMBOL (if applicable) AFIT/ENY	7a. NAME OF MONITORING ORGANIZATION							
6c. ADDRESS (City, State, and ZIP Code) Air Force Institute of Technology Wright-Patterson AFB OH 45433		7b. ADDRESS (City, State, and ZIP Code)							
8a. NAME OF FUNDING/SPONSORING ORGANIZATION	8b. OFFICE SYMBOL (if applicable)	9. PROCUREMENT INSTRUMENT IDENTIFICATION NUMBER							
8c. ADDRESS (City, State, and ZIP Code)		10. SOURCE OF FUNDING NUMBERS PROGRAM ELEMENT NO. PROJECT NO. TASK NO. WORK UNIT ACCESSION NO.							
11. TITLE (Include Security Classification) NUMERICAL SIMULATION OF COMPRESSIBLE VORTICES									
12. PERSONAL AUTHOR(S) Scott A. Morton, B.S., 1Lt, USAF									
13a. TYPE OF REPORT MS Thesis	13b. TIME COVERED FROM _____ TO _____	14. DATE OF REPORT (Year, Month, Day) 1989 December	15. PAGE COUNT 55						
16. SUPPLEMENTARY NOTATION									
17. COSATI CODES <table border="1"><tr><th>FIELD</th><th>GROUP</th><th>SUB-GROUP</th></tr><tr><td>C1</td><td>C1</td><td></td></tr></table>		FIELD	GROUP	SUB-GROUP	C1	C1		18. SUBJECT TERMS (Continue on reverse if necessary and identify by block number) Trailing Vortices	
FIELD	GROUP	SUB-GROUP							
C1	C1								
19. ABSTRACT (Continue on reverse if necessary and identify by block number) Thesis Advisor: Phillip S. Beran Instructor of Aerospace Engineering Department of Aeronautics and Astronautics									
20. DISTRIBUTION/AVAILABILITY OF ABSTRACT <input checked="" type="checkbox"/> UNCLASSIFIED/UNLIMITED <input type="checkbox"/> SAME AS RPT. <input type="checkbox"/> DTIC USERS		21. ABSTRACT SECURITY CLASSIFICATION UNCLASSIFIED							
22a. NAME OF RESPONSIBLE INDIVIDUAL Phillip S. Beran, Instructor		22b. TELEPHONE (Include Area Code) (513) 255-3517	22c. OFFICE SYMBOL ENY						

UNCLASSIFIED

A delta wing at a high angle of attack produces two vortices that generally undergo dramatic increases in core size, followed by the formation of regions of reversed flow. This phenomenon is called vortex breakdown and can have significant effects on the aircraft's lift, drag, and moment coefficients. The objective of this thesis is to provide a baseline model of the compressible vortex, independent of the complex body interaction with the delta wing. The model is then used to simulate vortex breakdown for various vortex strengths, Reynolds numbers, and Mach numbers with particular attention given to the effects of compressibility.

After running many simulations it was found that Mach number has a favorable effect by delaying vortex breakdown as defined above. Holding Reynolds number and vortex strength constant while increasing Mach number reduced the effective vortex strength while compressing the flow. Another important result of this compressible flow study was the disappearance of non-unique solutions at $Re = 200$ and $V = 1.0$ as Mach number was increased. No paths of non-unique solutions were found for $M > 0.2$.

UNCLASSIFIED